ADVANCED ARRAY IMAGING FOR BREAST AND

PROSTATE SONOGRAPHY

APPROVED BY SUPERVISORY COMMITTEE

Matthew A. Lewis, Ph.D.

Vikram Kodibagkar, Ph.D.

Roddy McColl, Ph.D.

Nikolai Slavine, Ph.D.

ADVANCED ARRAY IMAGING FOR BREAST AND PROSTATE SONOGRAPHY

by

RAVI SHANKAR VAIDYANATHAN

THESIS

Presented to the Faculty of the Graduate School of Biomedical Sciences

The University of Texas Southwestern Medical Center at Dallas

In Partial Fulfillment of the Requirements

For the Degree of

MASTER OF SCIENCE

The University of Texas Southwestern Medical Center at Dallas

Dallas, Texas

February, 2010

ACKNOWLEDGMENTS

I would like to express my primary thanks to Dr. Matthew Lewis, my mentor, for his sincere support, guidance and advice in both academic and personal areas. He was very supportive in helping me finish my course works. At several occasions has personally advised me on various things. It was a very good experience to work under him.

I would like to thank the program chair Dr. Peter Antich for accepting me in this program and give me a chance to get trained on various imaging modalities. He has advised me at many levels to help me complete this degree.

I would like to extend special thanks for Dr. Vikram Kodibagkar and Dr. Nikolai Slavine for advising me on various aspects of personality development. Their inputs are much appreciated.

I would like to thank Ms. Kay Emerson, the BME program assistant for helping me out with administrative issues and offering me valuable advices.

I would like to thank my parents and family.

Finally, I would like to thank my wife for her love and understanding.

TABLE OF CONTENTS

Chapter Page

I. INTRODUCTION 8

1.1 Ultrasound Imaging 8
1.2 Interaction of Ultrasound Waves with the Biological Media 11
1.3 Ultrasonic Tomography – frequency domain image reconstruction…… 13
1.4 Diffraction tomography Methods (Frequency domain imaging techniques)…14
1.5 Time-domain ultrasound imaging..... 19

II. REVIEW OF LITERATURE.....34

III. METHODOLOGY 40

IV. FINDINGS.....44

V. CONCLUSION AND FUTURE WORK 64

REFERENCES 71

LIST OF TABLES

Table	Page
1.1 Acoustic parameters for some biological materials	12

LIST OF FIGURES

Figure		Page
1	Monostatic setup of ultrasound tomography system.	20
2	Moving the transducer to various locations	20
3	Bistatic setup of ultrasound tomography system	26
4	Locations of the points of transmitter and receiver	26
5	Definition of an ellipse	27
6	Position vectors of the transmitter and the receiver	32
7	Line integral over circular paths of reflectivity	35
8	Exterior data acquisition	42
9	100X100 Shepp-Logan phantom	44
10	The corresponding sinogram	44
11	The reconstructed image from the obtained sinogram	44
12	The phantom used for partial reconstruction	45
12.1	A point source at origin	45
12.2	12.2 Sinogram of a point source at origin	45
12.3	Reconstruction of a point source	45
12.4	The phantom used for partial reconstruction.	45
13	The sinogram of figure 12	46
14	Reconstruction of figure 12	46
15	The sinogram obtained for an object placed exterior	47
16	The reconstruction with artefacts	47
17	100X100 binary phantom	47
18	Sinogram of figure 15	48
19	Reconstruction of figure 15	48
20	Phantom moved along positive x-axis	49
21	Corresponding reconstructions	49
22	Phantom moved along negative x-axis	50
23	Corresponding reconstructions	50
24	Phantom moved along positive y-axis	51
25	Corresponding reconstructions	51
26	Phantom moved along negative y-axis	52
27	Corresponding reconstructions	52
28	Phantom moved along the diagonal	53
29	Corresponding reconstructions	53
30	Objects placed next to the square	54
31	Corresponding sinogram	54
32	Reconstructed image of the phantom	54

33 Objects placed next to the square in the original binary phantom 55
34 Reconstructed image of the phantom 55
35 Objects placed in a random location on the top left quadrant 55
36 Reconstruction of Fig 35 55
37 Objects placed in a random location on the top left quadrant 56
38 Reconstruction of Fig 41 56
39 Error in reconstruction while phantom moved along x-axis 56
40 Error in reconstruction while phantom moved along y-axis 56
41 Error in reconstruction while phantom moved along the diagonal 57
42 Sinogram for the Shepp Logan for half projections in the radial direction 57
43 Reconstruction for the sinogram 57
44 Moving point source around the origin 59
45 Corresponding reconstructions 59
46 Moving the phantom to understand the symmetry in artifacts 61
47 Corresponding reconstructions 61

CHAPTER I

INTRODUCTION

1.1 Ultrasound Imaging

In conventional medical ultrasound such as B-mode imaging, the amplitude of the back-scattered ultrasound pulse is used to image tissues along a fixed beam direction[1]. This imaging technique works best in static organs, and it is difficult to image moving organs like the heart. The M-mode imaging technique is better for cardiac applications. For better image resolution, ultrasound tomography systems were developed in which ultrasound data were acquired by transducers placed in a circle around the object[2]. This task of deriving the structure of the object from scattered radiation is known as the inverse scattering problem.

The inverse scattering problem is known by several names like reflectivity tomography[3] and diffraction tomography[5, 6, 7] etc. Scattering refers to the effects on wave propagation due to an inhomogeneous medium. Since the inhomogenieties are unknown, the goal is to determine their properties – the spatial variation in density, compressibility, geometrical distribution etc. With the scattered wave field, determining the scatterer is called the inverse problem. As for the geometry of the scattering theory, the scatterer is assumed to

be present in a homogeneous reference medium with known properties. Following the notations used in Lehman[8], the acoustic pressure, p, in this medium satisfies the Helmholtz equation

$$(\nabla^2 + k^2)\, p(\mathbf{r}) = 0 \tag{1}$$

where the pressure field is given by

$$p(\mathbf{r},t)=p^0+p^1(\mathbf{r},t) \tag{2}$$

The ambient pressure, p^0 is constant. Since the scatterer is present in the reference homogeneous medium, the pressure field can be written as

$$p_0(\mathbf{r}) = p^{inc}(\mathbf{r}) + p^{sc}(\mathbf{r}) \tag{3}$$

where p^{inc} refers to the incident field and p^{sc} is the scattered field. In an ideal situation the incident pressure field is taken as a plane wave

$$p^{inc}(\mathbf{r}) = p^0\, e^{ikz} \tag{4}$$

where k is the complex wave number which is given by

$$k=(\omega/c)\,(1- i\omega M_\kappa) \tag{5}$$

where M_κ is the compressional viscosity.

Now, we are in a position to introduce the integral representations of the scattered field. In the region exterior to the scatterer, the pressure field is given by

$$(\nabla^2 + k^2)\, p_0(\mathbf{r}) = 0 \tag{6}$$

Introducing the Green's function

$$G(\mathbf{r} - \mathbf{r}') = e^{ik|\mathbf{r}-\mathbf{r}'|}/|\mathbf{r}-\mathbf{r}'| \tag{7}$$

that will satisfy the inhomogeneous impulse equation

$$(\nabla^2 + k^2)\, G(\mathbf{r} - \mathbf{r}') = -4\pi\delta(\mathbf{r}-\mathbf{r}') \quad (8)$$

Using one of the most frequently used approximations, the Rayleigh-Born approximation we can modify equation (7). At large distance the Green's function can be approximated by

$$G(\mathbf{r} - \mathbf{r}') \sim e^{ikr}/r \;\; e^{-ikr.\mathbf{r}'} \quad (9)$$

which holds true for $k_0 r'^2/r << 1$.

A Fourier diffraction theorem based reconstruction technique using the Born approximation is derived in Radial Reflection Diffraction Tomography (RRDT) [8]. Though my work is concerned with time-domain reconstruction techniques, I will discuss some existing frequency domain reconstruction techniques.

1.1.1 B-mode Imaging

B-mode (for Brightness mode) images are 2-D ultrasound images that contain pixels that correspond to ultrasound echoes. The value of the pixels corresponds to the amplitude of the echo. The image is obtained by sweeping narrow ultrasound through the object while detecting the echoes with a linear electronic array. In the B-mode image, the vertical position of the bright pixel is determined by the time-of-delay of the ultrasound wave and the horizontal position is determined by the location of the receiver. The path the echo follows is usually referred to as the beam line. The direction of the propagation along the beam line is called the axial direction and the direction perpendicular to this is called the

lateral direction. This technique also provides data at various levels enabling the creation of three-dimensional image.

The reconstruction technique may be compared to a crude backprojection of the obtained data without using any filter. In this way, B-mode imaging is considered very primitive form of ultrasound image reconstruction. Better techniques of reconstructing ultrasound data were later developed in the scheme of tomographic setup[2].

1.2 Interaction of Ultrasound Waves with the Biological Media

Ultrasound is the propagating disturbance of the properties (e.g., pressure and particle position) of the tissue through which it travels. Unlike electromagnetic radiation which can propagate in vacuum, ultrasound needs the material through which it travels. As a consequence this leads to interactions between the physical properties of the tissues and the extrinsic properties of the ultrasonic waves such as pressure. Acoustic properties of tissues as measured in many experiments were tabulated by Goss and Dunn[18, 19].
In medical imaging applications, the range of ultrasound frequencies used vary from 2-10 MHz (for imaging deep organs) to 40 MHz (for intrarterial imaging)[1]. In soft tissues

Material	Density (Kg/m^3)	Compressibility (10^{-12} m^2/Nt)	Velocity (m/s)	Acoustic Impedance (10^6 Kg/m^2s)
Fat	950	508	1440	1.37
Blood	1025	396	1570	1.61
Muscle	1070	353-393	1542-1626	1.65-1.74
Bone	1380-1810	25-100	27100-4100	3.75-7.4

Table 1.1 Acoustic parameters for some biological materials[9]

(which are predominantly water) like tendons and fat, the ultrasound propagation velocity is around 1500 m/s. Table 1.1 lists few of the acoustic parameters for some biological materials[9]. Though we notice the velocity of sound differs between materials, most of the time-domain reconstruction techniques assume the speed of sound to be constant, and the body is thus inhomogeneous in density. The speed of sound is related to the density and compressibility of the material in the following way:

$$c=1/(\rho\kappa)^{1/2} \tag{10}$$

where ρ is the density and κ is the compressibility. Now we are in a position to define the term *acoustic impedance* Z,

$$Z=\rho c \tag{11}$$

Variations in acoustic impedances cause specular reflection of the waves.

As mentioned earlier the spatial resolution of the ultrasound images depend on the frequency of the waves used (higher the frequency, better the resolution). But, higher frequencies also mean higher attenuation. So, there is always a trade-off depending on the organ of interest. In adult cardiology[1] 2.5-5 MHz is used to get enough penetration and for imaging of intravascular atherosclerosis, frequencies up to 40 MHz is used. The positioning of the transducers also plays an important role. For example, the nearest possible routes anatomically to place the transducers and image the prostate is transrectal and transurethral. This leads to various interesting geometries from a tomographic perspective for which no reconstruction algorithms exist.

1.3 Ultrasonic Tomography – frequency domain image reconstruction

So far the basics of ultrasonic imaging have been discussed. These ultrasound principles were used for a long time in conventional ultrasonic imaging developed for B-mode and M-mode imaging. One of the earliest works which used acoustic imaging in a tomographic setup, in the frequency domain, used algebraic reconstruction techniques (ART) [10, 11] to form images. Greenleaf used similar techniques to reconstruct the speed of sound using time-of-flight profiles[12]. Like most ART techniques the work was computationally intensive. Then there were techniques based on perturbation solutions of the wave equations[5]. These techniques reconstructed the speed of sound by approximating it by a small perturbation to velocity in the surrounding medium. Using

few first-order perturbation equations, images were reconstructed. There were old techniques that reconstructed spatial distribution of acoustical absorption with tissues from their two-dimensional projections[13], in a manner analogous to filtered backprojection.

1.4 Diffraction tomography Methods (Frequency domain imaging techniques)

There is another tomographic technique to reconstruct acoustic data called the diffraction technique. There are two important approximations that are used to approximate the wave equation, namely the Born[15] and the Rytov[16] approximations that transform homogeneous wave equation into nonhomogeneous equation using perturbation methods which can then be solved analytically which will include the effects of diffraction.

1.4.1 The Born approximation

Let us start with the Helmholtz equation and using the notations used by Lehman[8], we have

$$\nabla^2 \psi + K^2 \psi = 0 \tag{12}$$

If the total wave is the sum of incident and scattered wave, i.e.

$$\psi = \psi^{sc} + \psi^{inc} \tag{13}$$

then equation (12) can be written as

$$\nabla^2\psi^{sc}+k_0^2\psi^{sc}=O\psi^{inc} \quad (14)$$

where

$$O=- k_0^2(B^2-1) \quad (15)$$

and the object function,

$$B^2=k(x)^2/ k_0^2 \quad (16)$$

where k(x) is the wavenumber of the medium which varies spatially and k_0 is the wavenumber of the background medium. We arrived at equation (14) with an important assumption inherent with the Born approximation,

$$\psi^{sc}<<\psi^{inc} \quad (17)$$

that is, it assumes that the amplitude of the scattered energy is much less than the incident energy.

1.4.1 The Rytov approximation

Let us start again with wave equation (12) and substitute

$$\psi(\mathbf{r}) =\exp(i\, k_0\phi(\mathbf{r})) \quad (18)$$

where we express ψ in a form that assumes the information to be in the *phase* part of an exponential form, where complex phase allows for spatial variation in both propagation velocity and attenuation. The substitution results in

$$i\, k_0^{-1}\nabla^2\phi \; - \; |\nabla\phi|^2 + A^2=0 \quad (19)$$

where

$$A=1+\eta \tag{20}$$

where η is the change in refractive index. Now, let $\phi=\phi_0+\phi_1$ where ϕ_0 is the phase component of the pressure distribution $\psi(\mathbf{r})$ for no perturbation and where ϕ_1 is the phase perturbation due to perturbation in the refractive index. Substituting the perturbations into equation (19) we get,

$$i\, k_0^{-1}\nabla^2\phi_0+ i\, k_0^{-1}\nabla^2\phi_1-|\nabla\phi_0|^2-2(\nabla\phi_0.\, \nabla\phi_1) -|\nabla\phi_1|^2+1+2\eta+\eta^2 \tag{21}$$

Ignoring η^2 and $|\nabla\phi_1|^2$, we get,

$$\nabla^2(\phi_1 \exp(ik_0\phi_0)) + k_0^2(\phi_1 \exp(ik_0\phi_0))=i2k_0\eta \exp(i\, k_0\phi_0) \tag{22}$$

Equations (22) are the Rytov's approximation and it has the same form as equation (14). Equations (14) and (22) are both linear and their solution is a convolution of Green's solutions with the source terms for all space. The result is obtained by Tribolet[17].

1.4.2 Monostatic forward scattering model

To develop a linear forward scattering model for monostatic setup we start with the Helmholtz equation that governs the wave propagation and scattering,

$$[\nabla^2 + k^2(\mathbf{r})]\, \psi(\mathbf{r},\omega) = -p(\mathbf{r},\omega), \tag{23}$$

where $\mathbf{r}$ is given by the polar spatial coordinates $r(\cos\theta, \sin\theta)$ of a point in the surrounding medium, ω, the temporal frequency, $k(\mathbf{r})$ is the wavenumber of the medium, $\psi(\mathbf{r},\omega)$ is the total field, $p(\mathbf{r},\omega)$, the incident pulse temporal spectrum. To remove the

spatial inhomogeneity in equation (23), we add the background wavenumber, $k_0(\omega)= \omega/v_0$, to both sides of the equation and move the inhomogeneous term to the right hand side to obtain,

$$[\nabla^2 + k_0^2]\,\psi(\mathbf{r},\omega) = -p(\mathbf{r},\omega) - [k^2(\mathbf{r}) - k_0^2(\omega)]\,\psi(\mathbf{r},\omega) \tag{24}$$

Defining the object function as,

$$o(\mathbf{r}) = (k^2(\mathbf{r})/\, k_0^2) - 1 \tag{25}$$

equation (24) becomes,

$$[\nabla^2 + k_0^2]\,\psi(\mathbf{r},\omega) = = -p(\mathbf{r},\omega) - k_0^2(\omega)\, o(\mathbf{r})\, \psi(\mathbf{r},\omega) \tag{26}$$

where the term $k_0^2(\omega)\, o(\mathbf{r})\, \psi(\mathbf{r},\omega)$ is known as the secondary source which creates the scattered field. To convert equation (26) into an integration equation we have to use the Green's theorem[43]. Equation (26) now becomes,

$$\psi(\mathbf{R},\omega)=\int d\mathbf{r} G(\mathbf{R},\mathbf{r'},\omega)P(\mathbf{r'},\omega)+ k_0^2\,(\omega)\int d\mathbf{r'} G(\mathbf{R},\mathbf{r'},\omega)o(\mathbf{r'})\psi(\mathbf{r'}), \tag{27}$$

where the Green's function is given by,

$$G(\mathbf{R},\mathbf{r},\omega)= e^{ik0|\mathbf{R}-\mathbf{r}|}/4\pi|\mathbf{R}-\mathbf{r}| \tag{28}$$

The first integral in equation (27) is the primary field, $\psi^{inc}(\mathbf{R},\omega)$.Subtracting it from the total field yields the scattered field,

$$\psi^{scat}(\mathbf{R},\omega)= \psi(\mathbf{R},\omega)- \psi^{inc}(\mathbf{R},\omega)= k_0^2(\omega)\int d\mathbf{r} G(\mathbf{R},\mathbf{r},\omega)o(\mathbf{r})\psi(\mathbf{r}) \tag{29}$$

Evaluating the scattered field on the measurement surface, $\mathbf{r_0}$, we obtain,

$$\psi^{scat}(\mathbf{r_0},\omega)= k_0^2(\omega)\int d\mathbf{r} G(\mathbf{r_0},\mathbf{r},\omega)o(\mathbf{r})\psi(\mathbf{r}) \tag{30}$$

The above equation is nonlinear the scattering term is on both sides and is under an integral on the right hand side. Therefore to reconstruct an estimate of $o(\mathbf{r})$, we need to

simplify the equation by linearizing it. We can do it by assuming that the medium is weakly scattering and that the first Born approximation holds. Therefore equation (30) becomes

$$\psi_{\text{born}}^{\text{scat}}(\mathbf{r_0},\omega)= k_0^2(\omega)\int d\mathbf{r} G(\mathbf{r_0},\mathbf{r},\omega) o(\mathbf{r}) \psi^{\text{inc}}(\mathbf{r}) \quad (31)$$

We further assume the incident field is the results of a point source at $\mathbf{r_0}$, so that $p(\mathbf{r},\omega)=P(\omega)\ \delta(\mathbf{r_0}-\mathbf{r})$, where $P(\omega)$ is the incident pulse spectrum. With this assumption, the incident field is,

$$\psi^{\text{inc}}(\mathbf{r},\omega) = P(\omega)\ G(\mathbf{r_0},\mathbf{r},\omega), \quad (32)$$

and equation (31) becomes

$$\psi_{\text{born}}^{\text{scat}}(\mathbf{r_0},\omega)= P(\omega)\ k_0^2(\omega)\int d\mathbf{r} G^2(\mathbf{r_0},\mathbf{r},\omega) o(\mathbf{r}) \quad (33)$$

where the squared Green's function is the result of the transmitter and receiver being located at the same point. Using equation (28), the forward model of the monostatic setup is expressed as follows

$$\psi_{\text{born}}^{\text{scat}}(\mathbf{r_0},\omega)= P(\omega)\ k_0^2(\omega)/(4\pi)^2\int d\mathbf{r}\ e^{i2k0(\omega)|\mathbf{r_0}-\mathbf{r}|}/|\mathbf{r_0}-\mathbf{r}|^2\ o(\mathbf{r}) \quad (34)$$

We will see later how this model differs in a bistatic setup owing to the fact that the transmitter and locater are not colocated anymore.

1.4.1 Green's function for the Helmholtz equation

It is important to give a brief discussion of the Greens function of the Helmholtz's equation at this juncture for the case of 2-D and 3-D. A detailed explanation and

derivation of the all equations discussed in this section can be found in Barton[43]. Following the notations used by Barton[43], we have the Green's function for the operator in the wave equation $(-\nabla_{\mathbf{R}}^2 + ((1/c^2)\partial^2/\partial\tau^2$ where $\mathbf{R}= \boldsymbol{r}-\boldsymbol{r'}$ as they propagate is given by

Case I Three Dimensions

$$G_{0\tau}=\delta(\tau-R/c)/4\pi R \qquad (34.1)$$

This disturbance is expanding shell with radius τc. Beyond this point there is no trace of the disturbance which means there is no afterglow. Moreover, the Huygen's principle works in 3D.

Case II Two dimensions

$$G_{0\tau}= 1/2\pi(\theta(\tau-R/c))/ (\tau/[\tau^2-R^2/c^2]^{1/2} \qquad (34.2)$$

It can be seen that the impulse response rises steadily from zero to infinity. It becomes infinity at τ=R/c and diminishes after this point. IT diminishes and faces to zero which means there is an afterglow. The Huygen's principle does not work in 2D.

1.5 Time-domain ultrasound imaging

Time-domain image reconstruction techniques show how to reconstruct an image of a point reflecting object from broadband pulse-echo data generated by translating a single, omni-directional source-receiver over a suitable aperture. This means that the goal of a

broadband imaging system is to use the wide 'temporal' frequency bandwidth (generated by a large transmitting and receiving aperture), to obtain the complete information-

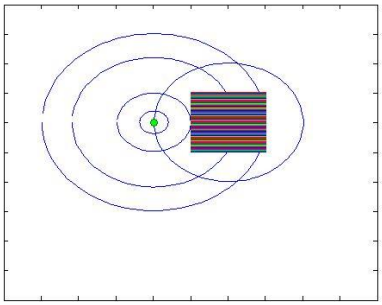

Figure 1. Monostatic setup of ultrasound tomography system. Shown here is the location of the point of transmitter/receiver (green) and few samples of radial projections.

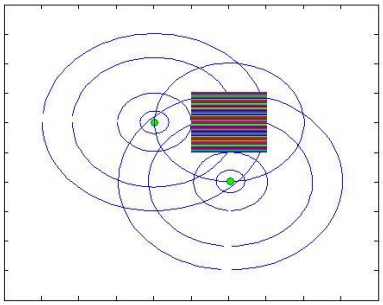

Figure 2. Moving the transducer to various locations (angular samples in addition to radial samples) on the circle, circular integrals are obtained over multiple intersecting paths.

bearing capacity of these signals. One of the earliest works which tackled the time-domain found in the work of Norton [20].To explain this monostatic model, where the same transducer acts as a transmitter and receiver (Figure 1), consider an infinitesimally short, spatially diverging pulse that is emitted into a two-dimensional weakly reflecting medium. If the reflected echoes are recorded at the same location (that is the location of the transmitter), as a function of time, line integrals of the property of the medium under study (e.g., reflectivity) over a family of concentric circles centered at this point are obtained. This model could be understood by observing that a diverging circular

disturbance produced by two-dimensional isotropic source, at any point in time, produces reflected waves simultaneously over the length of the arc illuminated by the wavefront at that point in time. These echoes arrive back at the receiver at the same instant of time where they are 'integrated' producing line integrals of the property of the medium over a family of concentric circles (as a function of time). Several such data are obtained by moving the transducer at various points (Figure 2) on the boundary (the boundary usually being a circle). The data obtained are reconstructed using various methods, one of the earliest being attempted in the work of Norton[20]. I will discuss some of the popular reconstruction techniques in the next chapter. Though these reconstruction techniques do not produce a perfect image because the system is limited by both finite temporal and spatial frequency bandwidth (limited spatial frequency bandwidth because of finite aperture), they improve the considerably improve the temporal-spatial system response compared to the conventional delay-and-sum method of imaging[21].

1.5.1 Photo/thermo acoustic imaging

Several time-domain reconstruction techniques are used in a hybrid modality imaging techniques known as a photo(thermo) acoustic imaging. Photoacoustic (PA) effect reported by Alexander Graham Bell[22] is the basis for PA imaging. The phenomenon is the generation of acoustic waves by the absorption of electromagnetic (EM) energy, such as radio-frequency (rf) waves[23]. Photoacoustic imaging uses the high EM contrast at high

ultrasound resolution in large volumes of biological tissues[24].Similar to the transducer setup described in the previous subsection for the monostatic geometry, the acoustic waves due to PA effect generated by the initial sources inside the tissue reach the boundary with various time delays. The image resolution as a function of imaging depth is depended upon the detected ultrasonic bandwidth[25].With the help of temporal PA signal, depth-dependent information of the object can be determined. This is called PA depth profiling[26].

Similarly, microwave induced themoacoustic imaging also exist in literature[27]. In this case, microwave pulses generate acoustic waves in a lossy medium. Although microwave-induced thermoacoustic imaging shares similar principles with photoacoustic imaging in the optical wavelength[28], it may have a wider use in medical imaging because microwaves penetrate deeper and more uniformly in biological tissues than light. Since, both these techniques in a tomographic setup share a similar model with the monostatic ultrasound tomography, we will consider only photoacoustic imaging.

1.5.2 Forward model based on spherical Radon transform

To image complex structures, in recent years, an imaging method called photoacoustic tomography (PAT) [29, 30] has caught wide attention. A forward model based for this imaging technique based on spherical Radon is similar to the monostatic ultrasound imaging.

Let the colored grid in figure 1 be a two-dimensional function $f(r,\theta)$ (describing for example, the reflectivity of the medium) defined in the inside of the circle of radius R. Let a short pulse of sound be emitted from a point (indicated in green color in figure 1) on the circumference at an angle ϕ measured from the positive x axis and the backscattered acoustic wave is recorded at the same point as a function of time. This generates line integrals over circles centered at this point. In other words, Spherical (or circular in two dimensional cases) Radon transformed projections. From a tomographic setup, this process of data acquisition is repeated on several points on the circumference (figure 2). The aim is to reconstruct $f(r,\theta)$ from circular integrals obtained from all the points on the circumference. To state symbolically, our aim is to reconstruct $f(r,\theta)$ from the following circular integrals:

$$g(\rho,\phi)= \int_{\ell(\rho,\phi)} f(r,\theta)\, ds \tag{23}$$

where $g(\rho,\phi)$ is the spherical Radon transform of $f(r,\theta)$. The path along which the function $f(r,\theta)$ is denoted by $\ell(\rho,\phi)$, which is a circle, parameterized by two variables ρ and ϕ, where ρ is the radius whose center lies on the point of measurement on the circumference of the enclosing circle at angle ϕ.

In a two-dimensional form equation (23) can be written in the following way:

$$g(\rho,\phi)= \int_0^{\infty} r dr \int_0^{2\pi} f(r,\theta) d\theta \text{ x } \delta\{[r^2 + R^2 - 2rR\cos(\phi-\theta)]^{1/2} - \rho\} \tag{24}$$

the delta function follows the circular path in the (r,θ) plane.

Equation (24) is the forward model based on the spherical Radon for monostatic ultrasound imaging. The same is applicable to photoacoustic imaging with a slight modification in the model. In the latter, there is no "emitter" because the acoustic waves are generated by a different mechanism (photoacoustic effect), but only the receiver. There are several reconstruction techniques to recover $f(r,\theta)$ which I will discuss in the next chapter.

1.5.3 Inverse source problem in photo/thermo acoustic tomography

As mentioned in the previous section, in the scheme of photoacoustic tomography, there are only receivers and no transmitters. Since, the acoustic waves are generated inside the object at some source, the problem of reconstructing the object from the data acquired by the receivers is called the "inverse source problem". Each temporal photoacoustic signal, measured at various locations of the receivers, provides one- dimensional radial information about the photoacoustic source relative to the receiver location. Often small-aperture receivers are used to approximate point detectors, which receive photoacoustic signals originating from spherical (circular in 2D) shells centered at each point detector, with the radius determined by the acoustic times of flight. For large aperture detectors, the reconstruction algorithms are different. One such reconstruction is attempted in [31]. Let us assume a heat source $H(\mathbf{r}, t)$, and a pressure to its response at position $\mathbf{r}$ and time t, $p(\mathbf{r}, t)$ in a homogeneous medium. Following the notations of Xu[24], the pressure would

follow the following wave equation, ignoring effects of thermal diffusion and kinematic viscosity[32]:

$$\nabla^2 p(\mathbf{r}, t) - 1/c^2\, \partial^2/\partial t^2\, (p(\mathbf{r}, t)) = -\beta/C_p\, \partial/\partial t\, (H(\mathbf{r}, t)) \tag{25}$$

where β is the isobaric volume expansion and C_p is the specific heat[33].

The solution to equation (25) is expressed by

$$p(\mathbf{r}, t) = \beta/4\pi C_p \iiint d^3r'/|\mathbf{r}-\mathbf{r}'|\; \partial/\partial t'\, (H(\mathbf{r}', t'))\;\; |_{t'=t-|\mathbf{r}-\mathbf{r}'|/c} \tag{26}$$

The heating function can be written as a product of two separable variables, spatial absorption function and the condition of thermal confinement,

$$H(\mathbf{r}, t) = A(\mathbf{r}) I_e(t) \tag{27}$$

Now equation (26) can be written as a convolution between the temporal profile $I_e(t)$ and the acoustic wave form $p_\delta(\mathbf{r},t)$ that is excited by an infinitesimally short pulse $\delta(t)$,

$$P_e(\mathbf{r}, t) = \int_{-\infty}^{\infty} I_e(t-\tau)\, p_\delta(\mathbf{r}, \tau)\, d\tau \tag{28}$$

where

$$p_\delta(\mathbf{r},t) = \partial/\partial t[\; 1/4\pi \iint_{|\mathbf{r}-\mathbf{r}'|=ct} p_0(\mathbf{r}')\, d\Omega'\;], \tag{29}$$

where $d\Omega'$ is the solid-angle element of vector $\mathbf{r}'$ with respect to the point at $\mathbf{r}$; and $p_0(\mathbf{r})$ is the initial pressure excited by a $\delta(t)$ electromagnetic source, computed by $p_0(\mathbf{r})=\Gamma(\mathbf{r})A(\mathbf{r})$, which acts as the source for the propagating acoustic wave.

Let us assume a very simple electromagnetic source $\delta(t)$, and the photoacoustic signal is detected at the location $\mathbf{r}_0$ by a point detector. The signal detected at that transducer can be symbolically written as,

$$P_d(\mathbf{r}_0,t)= \partial/\partial t[\ 1/4\pi \iint_{|\mathbf{r}-\mathbf{r}'|=ct} p_0(\mathbf{r})\ d\Omega\ ] \tag{30}$$

where $d\Omega$ is the solid-angle element of vector $\mathbf{r}$ with respect to the point at $\mathbf{r}_0$.

The goal is reconstruct $p_0(\mathbf{r})$ from the acquired data $P_d(\mathbf{r}_0,t)$.

1.5.4 Relationship between the acquired data and the Radon transformed projections

Rewriting equation (30), we obtain,

$$F(\mathbf{r}_0,t)= 4\pi/t \int_0^t P_d(\mathbf{r}_0,t)\ dt = \iint_{|\mathbf{r0}-\mathbf{r}'|} p_0(\mathbf{r})\ d\Omega \tag{31}$$

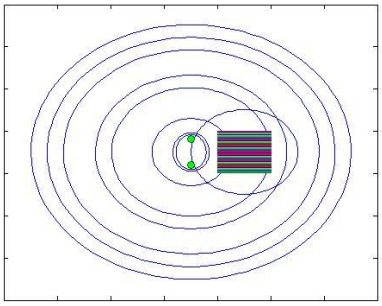

Figure 3. Bistatic setup of ultrasound tomography system. Shown here is the locations of the points of transmitter and receiver (green) and few samples of "radial" projections.

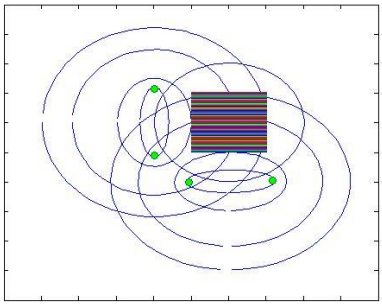

Figure 4. Bistatic setup of ultrasound tomography system. Shown here is the locations of the points of transmitter and receiver (green) at various angular positions and few samples of "radial" projections.

The function $F(\mathbf{r}_0,t)$ gives the spherical Radon transformed projections of $p_0(\mathbf{r})$. $\mathbf{r}_0$ is the location of the detectors which is usually on a circumference of a circle centered at the center of the object and t is the time at which "radial" projections are obtained.

The Radon transform approximation yields good results for circular detection geometry. All the reconstruction techniques existing for the circular detection geometry hold well only when the center of the object is centered at the center of the circle. Significant artifacts appear when the source deviates from the center. Another important assumption in most of the time-domain reconstruction techniques is that the speed of sound, c, is constant inside the medium. This assumption is reasonable because the variation in the speeds of sound in biological medium is very less.

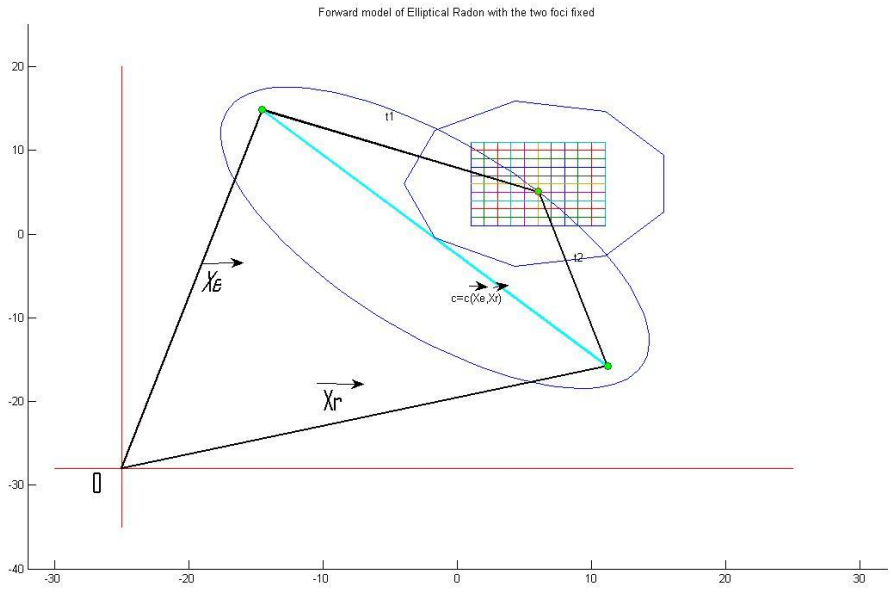

Figure 5. Definition of an ellipse. As can be seen from the figure, an ellipse has five degrees of freedom.

There are other approximations which have been attempted wherein a 2D Radon transform was approximated with a Hilbert transform[37]. The most common form of reconstruction, backprojection for tomographic data, will be discussed later.

1.5.5 Bistatic time-domain ultrasound imaging (Elliptical Radon transform-based imaging)

Unlike monostatic setup in ultrasonic imaging, in bistatic setup the locations of the source and the detector differ. In this respect, monostatic imaging can be considered a special case of bistatic imaging. Whenever the source and the sensors are not at the same location, surfaces of constant time of flight are ellipses, whose foci are the locations of the transmitting and receiving transducers.

Some conventional medical imaging systems like focus-and-steer imaging[34] and synthetic-focus imaging[35] with complete dataset include the effects of backscattered signals acquired by detectors not at the same location as the source. Image reconstruction using elliptical projections can also be found in applications like Synthetic Aperture Radar (SAR) imaging[36]. The geometric setup used in this modality is not appropriate for medical imaging.

A. Parameters of an ellipse and the elliptical Radon

Consider an ellipse (Figure 5) with foci at $\mathbf{x_e}$ and $\mathbf{x_r}$. The family of ellipses at these foci has semi-major axis *a*, semi-minor axis *b* and a foci separation of $2c=|\mathbf{x_e} - \mathbf{x_r}|$. The vector form of ellipse can be written as

$$|\mathbf{x}-\mathbf{x_e}| + |\mathbf{x}-\mathbf{x_r}| = 2a \tag{32}$$

Next, we make an identity linking the *a* and *c* with the *eccentricity e* of the ellipse,

$$a=c/e \tag{33}$$

implying,

$$|\mathbf{x}-\mathbf{x_e}| + |\mathbf{x}-\mathbf{x_r}| = 1/e\ |\mathbf{x_e}-\mathbf{x_r}| \tag{34}$$

e is defined the domain $0 \leq e < 1$.

One possible definition of elliptical Radon would therefore be

$$R_{\mathbf{xe,xr}}(e) = \int_{|\mathbf{x}-\mathbf{xe}| + |\mathbf{x}-\mathbf{xr}|=1/e\ |\mathbf{xe}-\mathbf{xr}|} f(\mathbf{x})\ ds \tag{35}$$

There are five parameters in this expression. If we additionally require that the semi-major axis be orthogonal to a line, then the number of degrees of freedom can be reduced to four. At present, nothing is known about the analytical inversion of this transform. Even a Fourier slice theorem is lacking. The earliest known approximate reconstruction was attempted in 1989[38].

To define the elliptical Radon, consider the locations of a transmitter and a receiver on *xy* plane on the *y* axis with y coordinates +/- *d* from the origin. Then a pulse moving from the transmitter to the receiver from a point (*x*, *y*) in the plane travels a distance A:

$$A = \sqrt{h^2 + (y+d)^2 + x^2} + \sqrt{h^2 + (y-d)^2 + x^2} \tag{36}$$

The signal arriving at the receiver at a time instant t=A/c is that due to all signals which have traveled a distance A. the geometry dictates that the signal must have reflected from the loci in the xy plane given by a re-arrangement of equation (36):

$$x^2 + y^2 = (1-4d^2/A^2) = A^2/4 - d^2 \tag{37}$$

which is an ellipse centered at the origin with A and d being constants.

To convert the expression from time-dependent equation to a spatial one, we introduce a new variable $r^2 = A^2/4 - d^2$, we have

$$x^2 + y^2(r^2/\, r^2 + d^2) = r^2 \tag{38}$$

where the semi-minor axis which lies on the x axis and is of length r and the semi-major axis lies on the y axis and is of length

$$y_r = r\sqrt{(r^2 + d^2)/r^2} \tag{39}$$

It can be seen clearly, when d=0 (monostatic case), $y_r = r$ which is the same length as the semi-minor axis, indicating the geometry is a circle. The aspect ratio of the ellipse is defined as the ratio of its semi-minor axis to the semi-major axis. It can been that the aspect ratio of the ellipse defined above changes smoothly from $\sqrt{1+d^2}$ for small r to 1 for a circle. The ellipse will start appearing like a line for large d.

If the ellipses are parameterized using polar coordinate,

$$x = r\cos\theta \tag{40}$$

$$y = r\sqrt{(r^2 + d^2)/r^2}\sin\theta \tag{41}$$

then the "elliptical" measurement at the receiver, with ellipse centered at the origin, and the time corresponding to the radius r, is

$$F(r) = \int_{-\infty}^{\infty} \int_{\infty}^{\infty} f(x,y)\delta(x^2+y^2\,(r^2/r^2+d^2) - r^2)\, dxdy$$

$$= r \int_{0}^{2\pi} f(r\cos\theta, r\sqrt{(r^2+d^2)/r^2}\ \sin\theta)\sqrt{1+(d\cos\theta/r)^2}\, d\theta \qquad (42)$$

where the differential length dl of the line integral is written in terms of the integration variable $d\theta$ as:

$$dl = r\sqrt{1+(d\cos\theta/r)^2} \qquad (43)$$

Equation (42) gives a generalized elliptical Radon transform.

B. An engineering derivation of the elliptical Radon model from the time-dependent wave equation

Starting with the wave equation in the time-domain, we have

$$(\nabla^2-\partial_{tt})\, u(\mathbf{r},t) = s(\mathbf{r},t) \qquad (44)$$

For a non-zero eigenvalue, the Green's function exists, given by

$$LG\,(\mathbf{x}, \mathbf{x'}) = \delta(\mathbf{x}-\mathbf{x'}) \qquad (45)$$

where $L=(\nabla^2-\partial_{tt})$, and

$$Lf(\mathbf{x})=s(\mathbf{x}) \qquad (46)$$

which implies,

$$f(\mathbf{x})=\int_{B.C} s(\mathbf{x'})\, G(\mathbf{x},\mathbf{x'})\, d\mathbf{x'} \tag{47}$$

Now,

$$(\nabla^2-\partial_{tt})p(\mathbf{r},t,\mathbf{r'},t')=\delta(\mathbf{r}-\mathbf{r'}) \tag{48}$$

$$p(\mathbf{r},t,\mathbf{r'},t')=1/(4\pi|\,\mathbf{r}-\mathbf{r'}|)\,\delta(t-t'-|\mathbf{r}-\mathbf{r'}|) \tag{49}$$

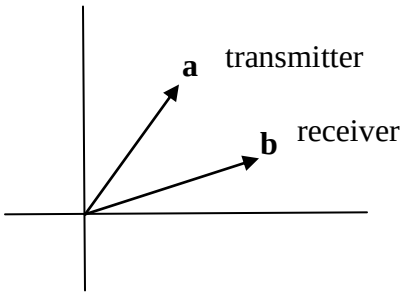

Figure 6. Position vectors of the transmitter and the receiver which act as the foci of the ellipse

We use $p(\mathbf{r},t,\mathbf{r'},t')$ to propagate signal from source to scatterer, and then from scatterer to receiver. Using the implicit Born approximation for single scatterer, we calculate incident field,

$$(\nabla^2-\partial_{tt})\,u_i(\mathbf{r},t)=\delta(\mathbf{r}-\mathbf{a})\,\delta(\mathbf{t}-\mathbf{0}) \tag{50}$$

scattered field,

$$(\nabla^2-\partial_{tt})\,u_s(\mathbf{r},t)=o(\mathbf{r})u_i(\mathbf{r},t) \tag{51}$$

Using the positional vectors, we derive,

incident field,

$$u_i(\mathbf{r},t)=p(\mathbf{r},t,\mathbf{r'}=\mathbf{a},t'=0)= 1/(4\pi|\ \mathbf{r}-\mathbf{a}|)\ \delta(t - |\mathbf{r}-\mathbf{a}|) \quad (52)$$

and the scattered field,

$$(\nabla^2-\partial_{tt})\ u_s(\mathbf{r},t)= s(\mathbf{r},t) \quad (53)$$

where,

$$s(\mathbf{r},t)= 1/(4\pi|\ \mathbf{r}-\mathbf{a}|)\ o(\mathbf{r})\ \delta(t - |\mathbf{r}-\mathbf{a}|) \quad (54)$$

where $o(\mathbf{r})$ is the scattering object.

Solving for the scattered field, we get,

$$u_s(\mathbf{b},t)= \int_{t',\mathbf{x}} s(\mathbf{r},t)\ G(\mathbf{b},t,\mathbf{r},t')d\mathbf{x} = 1/(4\pi)^2 \int o(\mathbf{r})/|\mathbf{r}-\mathbf{a}|\ \delta(t - |\mathbf{r}-\mathbf{a}|)\ \delta(t-t'- |\mathbf{b}-\mathbf{r}|)d\mathbf{x}dt \quad (55)$$

where

$$\delta(t - |\mathbf{r}-\mathbf{a}|)\ \delta(t-t'- |\mathbf{b}-\mathbf{r}|) =\delta(t - |\mathbf{r}-\mathbf{a}|- |\mathbf{b}-\mathbf{r}|) \quad (56)$$

Equation (55) gives the wave form in time-domain as an elliptical Radon transformed projection..

CHAPTER II

REVIEW OF LITERATURE

The problem of recovering a function from a subset of its spherical means, which has applications in both photo/thermo acoustic tomography and monostatic imaging, has been of interest to applied mathematicians and engineers for several years. One of the first works to tackle this problem was the seminal paper also by Norton[39]. The author was interested in the problem in the scheme of ultrasound reflectivity problem and this paper dealt with the geometry where spherical radon transformed projections are obtained on locations on a circumference of a circle. In an earlier paper[20] by the same author, the same line-integral model was used for an analysis of a reflectivity reconstruction problem. But here, the problem was analyzed for the case of an omni-directional source-receiver moved along a straight line in the boundary of a half-plane. That kind of a modeling would be appropriate for Synthetic Aperture Radar (SAR) imaging. During the time his paper was published[39], most of the acoustical imaging systems in medical diagnosis employed highly directional sources and receivers (like the traditional single probe system) to provide resolving power transverse to the direction of propagation whereas the solution to the reflectivity reconstruction problem in his paper was the basis for a high-resolution, tomographic imaging techniques that employs omnidirectinal transducer elements like the one shown in Figure 6.

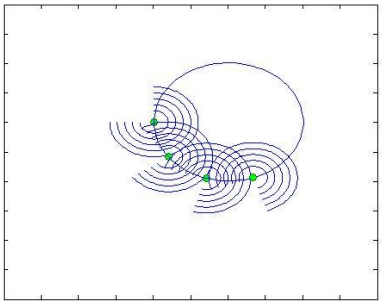

Figure 7. When an omnidirectinal element sends out a pulse and measure the echoes back as a function of time, line integral over circular paths of reflectivity are measured.

The reconstruction to the problem is obtained by deriving a relationship expressing the all the circular harmonic coefficients of the function to be recovered in terms of the projections obtained at each angular location. This, approach, which may be termed the method of circular harmonic decomposition, is possible because of the problem's inherent circular symmetry. That is precisely the reason why the same approach cannot be done with elliptical Radon transformed projections because they lack symmetry. Then a Hankel transformation is performed on each harmonic coefficient to yield the corresponding harmonic coefficient of the original function. Finally, the function is recovered by inserting the harmonic coefficients into the angular Fourier series. In essence, the method suggested in this paper can be made to resemble a convolution-backprojection operation. It is easy to perceive that as the radius of the enclosing circle becomes large relative to the size of the object, the integration paths intersecting the object approach straight lines. In that case the convolution-backprojection formulation reduces to that of conventional computerized x-ray tomography.

As mentioned previously, if the measurements are made in the far field with respect to the scattering region, where the Born approximation is usually applicable, then the scattering distribution and the scattering measurements bear a simple Fourier transform relationship to each other[41]. But in a practical medical imaging system Born approximation is impractical because the far-field approximation imposes unreasonable constraints on imaging distances. Without the far-field approximation exact inversion formulas are obtained by some authors using monochromatic illumination[42.] But these solutions are derived under the assumption of weak scattering using the first-order Born or Rytov approximations as mentioned in the previous chapter. But a three-dimensional inverse scattering problem was examined for the more general case of broad-band illumination without a far-field approximation[40]. Here, broad-band omnidirectional spherical waves are assumed to be the incident waves.

In frequency domain, there is another wave-based tomographic imaging algorithm that was developed based upon a single rotating radially outward oriented transducer[8]. The geometrical setup is similar to the one shown in Figure 2. But since this is a frequency domain imaging technique, a spherical Radon model is not appropriate, but the acquisition of data is very similar to it. At each angular location at a fixed radius, the transducer launches a primary field and collects the backscattered field in what is called a "pitch/catch" operation. This is similar to the medical intravascular ultrasound systems (IVUS). IVUS systems use conventional ultrasound imaging called the B-mode imaging. Goss[8] develops a wave-based imaging algorithm using diffraction tomography

techniques. In his work a mutimonostatic mode is used for data acquisition. Mutimonostatic is a terminology used when a single transducer is rotated along the circumference of the circle as opposed having many transducers on a circle and sending and receiving signals at the same time. The implementation of this model reduces the hardware resources and also interference effects of acoustic waves. The author derives an analytic expression for the multimonostatic inverse and uses Hilbert space inverse wave algorithm to construct images.

In recent years researchers have taken interest time-domain reconstruction algorithms based on spherical Radon transformed model because if its applications in photo/thermoacoustic tomography. A limitation of these methods is that the Radon transform model is appropriate only when then medium is insonified by an impulsive (infinite bandwidth) wave. When pulses of finite bandwidth are employed, image quality can be compromised significantly[44]. But the existing frequency-domain algorithms provide high quality images for many numbers of discrete frequencies that is computationally very demanding. Some authors have worked on time-domain waveform for inverse scattering methods by the method of frequency decomposition to work the spatial Fourier transform[46] and others on quantitative time-domain imaging[45].

The earliest known spherical Radon transform based image reconstruction was investigated by Norton[39]. The paper was based on circular harmonic decomposition.

But only recently, a paper provided a filtered-back projection (FBP) based reconstruction for the spherical Radon transformed data in 2-D[47]. FBP algorithms for 3-D have existed for a longer time. The authors provide a log-based filter to invert spherical Radon transformed data in even dimensions. If the spherical Radon transform *Mf* of a function *f* is defined in the following way,

$$(Mf)(x,r)=1/|S^{n-1}|\int_{S^{n-1}} f(x+r\theta)\, dS(\theta) \tag{57}$$

where $|S^{n-1}|$ denotes the area of S^{n-1} in $\mathbf{R}^n$ and ds (θ) denotes the area measure on the sphere which in two-dimensions would be arcs.

The reconstruction formula suggested in the Finch[47] paper is (following the notations of the paper),

$$f(x)= 1/2\pi R_0 \int_S \int_0^{2R_0} \partial_r r \partial_r (Mf)(p,r) \log |r^2 - |x-p|^2| \, dr ds(p) \tag{58}$$

where R_0 is the radius of the circle on which the detectors are placed, *p* is the angular location of the detectors and *r* is the radius over which the circular integrals are measured with *p* as center.

An explicit representation for the wave is given in terms of the spherical radon transform,

$$u(p,t)=1/(n-2)!\partial_t^{n-2} \int_0^t r(t^2 - r^2)^{(n-3)/2} (Mf)(p,r) dr \tag{59}$$

where *n* gives the dimension. Interesting to note here is that this solution to the initial value problem gives *u* as a function of time *t*, whereas the conventional image reconstructions are for a constant time.

One of the earliest attempts to reconstruct elliptical Radon transform data approximately was attempted in[38]. Each elliptical Radon transformed projection is back projected with a weight that is equal to the product of the distance of a point on the ellipse from the two loci. Recently, authors have attempted[48] a Fourier transform based image reconstruction for ellipsoidal projections. The work does not clearly define and explain the elliptical Fourier transform.

CHAPTER III

METHODOLOGY

In the background section we saw several formulas to reconstruct a function from the spherically Radon transformed data. In theory all these formulas assume continuous functions. In real applications that would mean obtaining infinite amount of data which is practically not feasible. For example, we can have only a fixed number of detectors for the monostatic setup or move a single transducer at fixed number of angular locations. For the monostatic setup, the numerical implementation of the filtered backprojection algorithm derived in[47] 100 equally spaced angular samples and 100 equally spaced radial samples were used.

The discrete version of the forward problem[47] can be stated as follows,

$$F^{k,m} = (Mf)\,(p^k, r^m), \tag{60}$$

where F is the spherical Radon transformed projections, p^k is the angular location given by,

$p^k = R_0(\cos(kh_\phi), \sin(kh_\phi))$ where k runs from 0 to 100 in steps of 1 and $r^m = mh_r$ where h_ϕ is the angular spacing given by 0.0622 radians (2π divided by angular samples) and h_r is the radial spacing which is equal to 1.4142 "pixel" units. The radius of the circle R_0 on which the transducers are placed are determined by half of the diagonal of the size of the square object which is 100 pixels each side. The radial spacing is obtained by dividing the diameter of this circle by the number of radial samples.

To implement equation 58 to reconstruct the function we need to calculate the partial derivative with respect to r. To be exact, we need to calculate the $\partial r + r\partial_r^2$ of the obtained

projections. To discretize differentials, we approximate with symmetric finite differences of the samples in the projection $F^{k,m+1}$-$F^{k,m-1}$/2 h_r and for the second order partial derivatives, we use $F^{k,m+1}$-$F^{k,m-1}$-2$F^{k,m}$/ h_r^2. The discrete version of the entire expression of ∂r+r∂_r^2 acting on the projection would be as follows,

$$1/\ h_r((m+1/2)\ F^{k,m+1} + (m\text{-}1/2)F^{k,m-1} - 2mF^{k,m} \tag{61}$$

where $F^{k,-1}$=$F^{k,Nr+1}$=0 because of the boundary conditions.

Now, the integration along circular paths over all angles is performed by linear spline interpolation, interpolating the projections at the positions r^m. The discrete version of the interpolation operator is defined as follows

$$T^k[G](r)= F^{k,m}+ r\text{-}r^m/h_r(F^{k,m+1}\text{-}F^{k,m}) \tag{62}$$

where r is in between two consecutive radial samples r^m and r^{m+1}.Therefore the discrete version of the entire equation (58) is as follows

$$\sum_{m'=0}^{Nr-1} a_{m,}^{m} F^{k,m'} + 1/h_r \sum_{m'=0}^{Nr-1} b_{m'}^{m} (F^{k,m'+1} - F^{k,m'}) \tag{63}$$

where

$$a_{m,}^{m} = [\{r - r^m) \log\ |r - r^m\ | + r + r^m \log\ |r + r^m\ | - 2r]_{r=r^{m'}}^{r^{m'}+1} \tag{64}$$

$$b_{m'}^{m} = -r^{m'} a_{m,}^{m} + 1/2[(r^2 - (r^m)^2) \log\ |r^2 - (r^m)^2\ | - r^2]_{r=r^{m'}}^{r^{m'}+1} \tag{65}$$

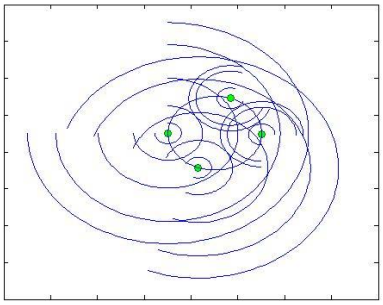

Figure 8. Exterior data acquisition. If the object is at the top right of the ring of detectors, the detectors on the left half of the ring will have a higher radial spacing than the right half

Finally, the discrete version of the back-projection operator[47] is given by

$$1/(N_{\phi}+1)\sum_{k=0}^{N_{\phi}} F(|\, x^{i} - p^{k}\,|)\,, \quad x^{i} \epsilon\, D \tag{66}$$

The computational efforts are $O(N^3)$ for the FBP because all $(N+1)^2$ reconstructions for the points in the image, $N_{\phi}+1$ summations must be done. Here $N=N_{\phi}=N_r=100$. The reconstructions were performed when both the object was inside the ring of detectors and exterior to it. In the exterior case, there were more radial samples from one half of the ring of detectors like shown in Figure 7. In this case, the object to be reconstructed is on the top right of the ring of detectors; the detectors on the left half of the ring of detectors will have more radial spacing than the right half. The radial spacing increase proportionately as the distance between the ring of detectors and the object increases. For the bistatic case, the distance between the transmitter and the receiver remain constant throughout data acquisition. This would geometrically mean that the distance between the two foci of the ellipse remain constant. In addition, a further constraint was imposed that the major axis remains tangential to the circle on which the pair of transducers are rotated. The center of the ellipse, the mid-point of the major axis is the angular location e^k, where k runs from 0 to 100 with an angular spacing of 0.0622 radians.

We are at a position to define the eccentricity ϵ of an ellipse. If the major axis of the ellipse is *a* and the minor-axis *b*, then the eccentricity is defined as a follows

$$\epsilon = \sqrt{1 - (b/a)^2} \tag{67}$$

And the distance from the center to either focus is *ae* which is equal to $\sqrt{a^2 - b^2}$. In my numerical implementation of the forward model, the distance between the foci remains constant. If the constant is *c*, then for linear samples of major axes $a^m = ma_r$, where *m* runs from 0 to 100 in steps of 1 (a_r=1), then the samples of minor axes are calculated as follows,

$$b^m = \sqrt{(a^m)^2 - c^2} \tag{68}$$

which means the samples of minor axes do not increase in a linear fashion.

For the backprojection, the projections were smeared aback along elliptical arcs with the filter that was used in the monostatic setup. Here, the log based filter had values of samples of minor axes as opposed to the radial samples in the case of mono-static setup. In the case of multi-bi-static setup, where there are more than one receiver per transmitter, the filter contained samples of eccentrities of the ellipses instead of the radial samples. In this case, the eccentrities start from zero (where an ellipse is a circle) and approach towards the value 1 as a the receiver moves farther away from the transmitter on a circle and moves back to the value 0 as the pair of transducers get closer.

CHAPTER IV

FINDINGS

In this section, I will present the results for the FBP reconstructions of phantoms for various geometrical setups. For the monostatic setup, a 100X100 Shepp-Logan phantom was used (figure 9).

Figure 9. 100X100 Shepp-Logan phantom

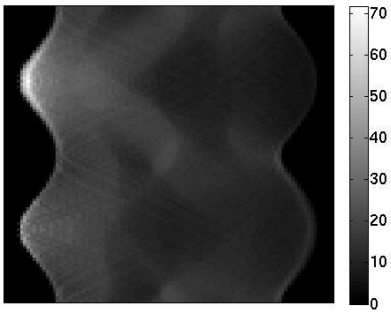

Figure 10. The corresponding sinogram of the phantom

For $N=N_{\phi}=N_r=100$, for a total angular data acquisition of 360 degrees, the corresponding sinogram of the Shepp-Logan phantom is shown in Figure 10.

The reconstructed image using the FBP algorithm mentioned in the methodologies section is shown in Figure 11.

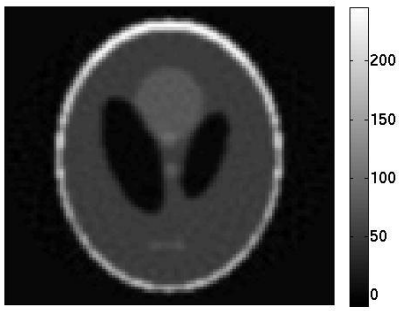

Figure 11. The reconstructed image from the obtained sinogram using the FBP method

The following image shows the reconstruction of a point source (Figure 12).

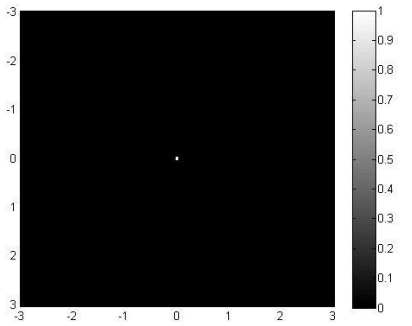

Figure 12.1 A point source at origin

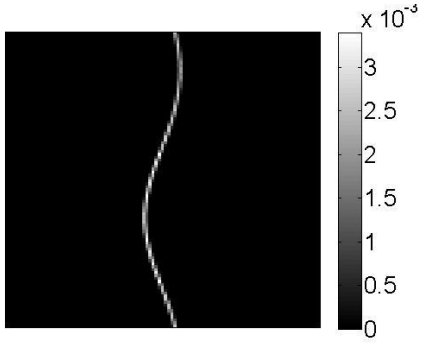

Figure 12.2 Sinogram of a point source at origin

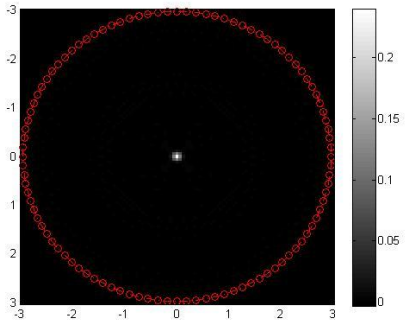

Figure 12.3 Reconstruction of a point source

Next, for the phantom shown in Figure 13, the algorithm was used to reconstruct the

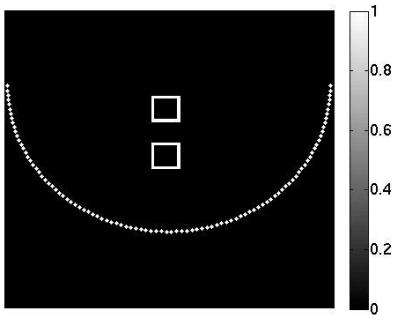

Figure 12.4 The phantom used for partial reconstruction. The location of the detectors is shown with white dots.

object from half the data. This kind of modeling is most appropriate for breast cancer imaging using the tomographic modality. The corresponding sinogram and the reconstruction are shown in Figures 14 and 15 respectively. In this case $N=N_{\phi}=N_r=100$ with an angular coverage of 180 degrees.

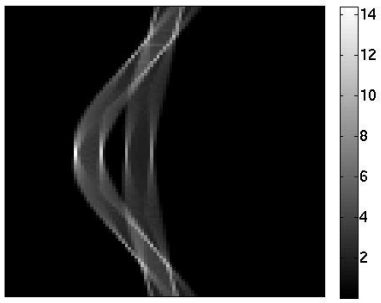

Figure 13. The sinogram of the phantom shown in Figure 10 for partial angular coverage

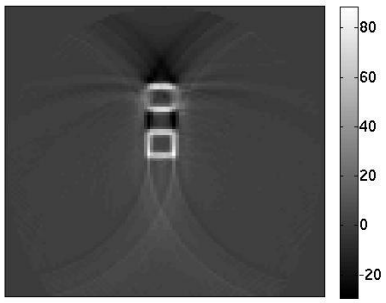

Figure 14. Reconstruction of phantom shown in fiure 10 for partial angular coverage

For the case of exterior reconstruction, where the object was placed exterior to the ring of detectors (top right to the ring of detectors, with the center of the object 2N pixels from the center of the ring of detectors with radius of $\sqrt{2}$ N pixels. In this case $N= N_{\phi}= N_r=100$ but the radial spacing for the detectors on the left half is twice that of the right half. The phantom used is shown in Figure 7 and the corresponding sinogram is shown in Figure 16 and the reconstruction using FBP is shown in Figure 17.

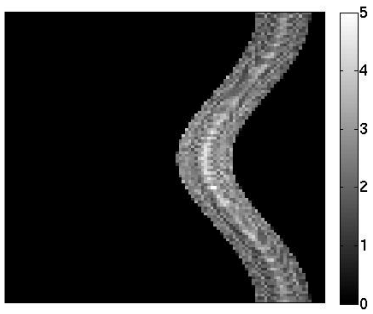

Figure 15. The sinogram obtained for an object placed exterior of the ring of detectors

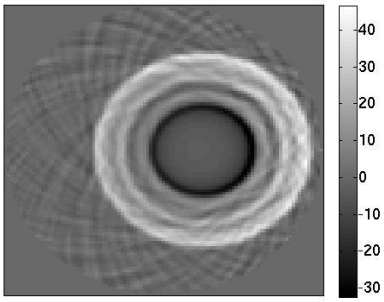

Figure 16. The reconstruction with artefacts for the exterior case.

To understand the behavior of the filter for the bistatic case, a different phantom was used as shown in Figure 18. It is a 100X100 binary phantom with a square in the middle of the phantom of 100 pixels each side.

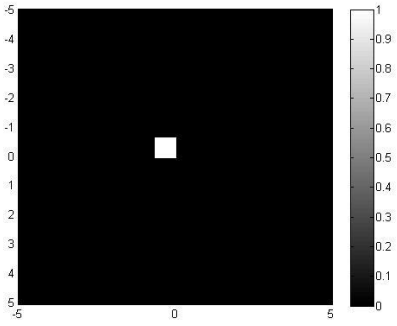

Figure 17. 100X100 binary phantom used with a square in the middle of 10 pixels each side.

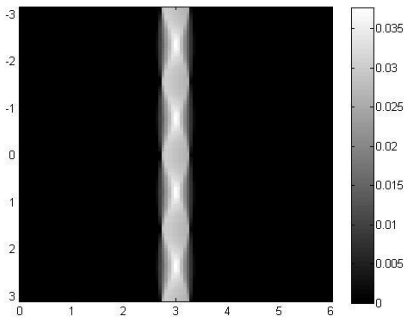

Figure 18. Sinogram of the phantom shown in Figure 15

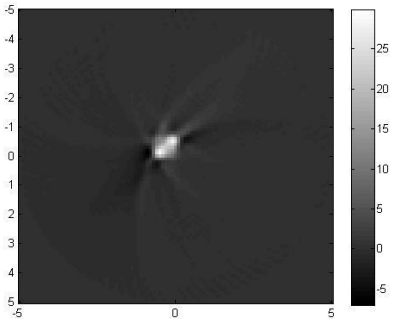

Figure 19. The reconstructed object

For N= N_{ϕ}= Na=100, and for a angular coverage of 360 degrees, the corresponding sinogram is shown in Figure.19. The reconstructed object is shown in Figure 20. Since, the filter is a 'computational' quantity and to understand its spatial behavior, the square on the binary phantom was spatially moved. The following images were moved along the x-axis with no change in the y-axis. The image was moved every 2-pixels on either side of the center. To conserve space, few are shown here. A graph comparing the spatial location and the error in reconstruction will follow.

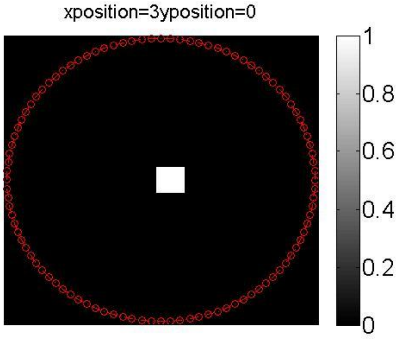

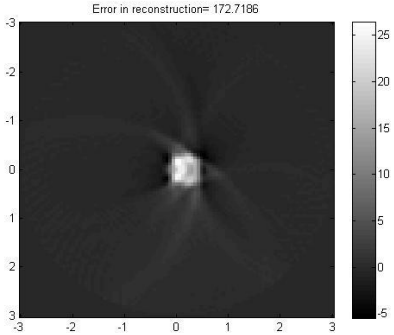

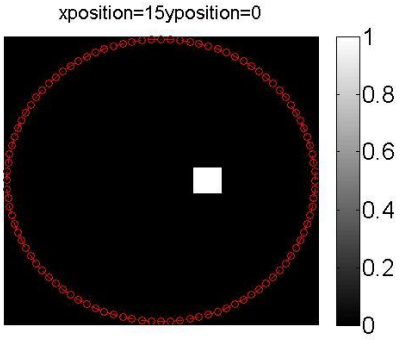

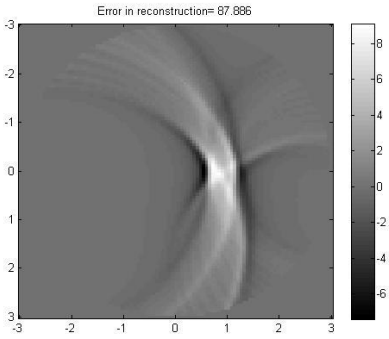

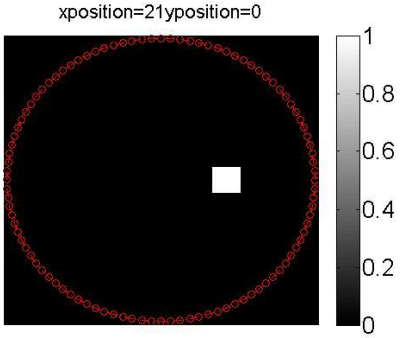

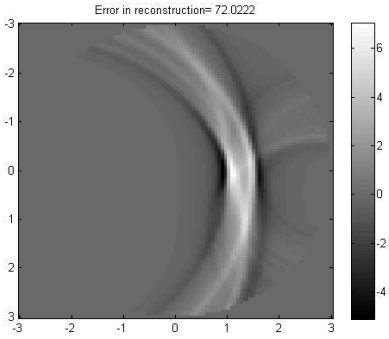

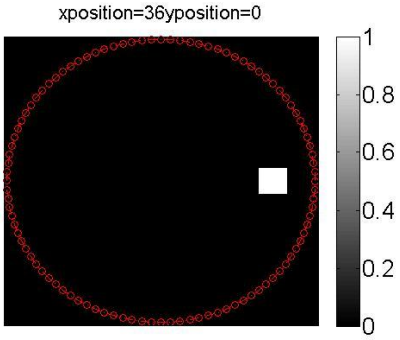

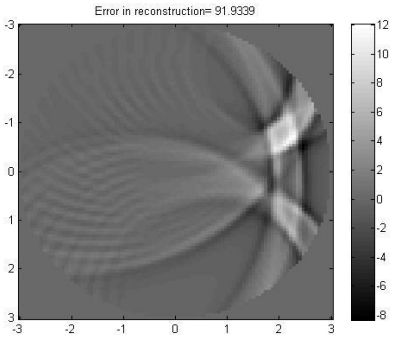

Figure 20. Phantom moved along positive x-axis while no change in y-axis

Figure 21. Corresponding reconstructions

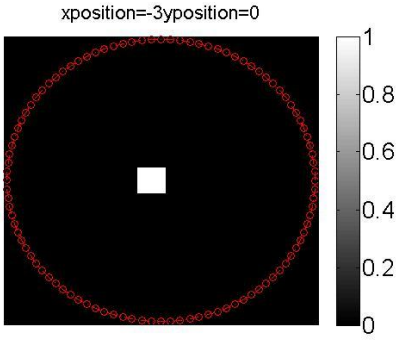

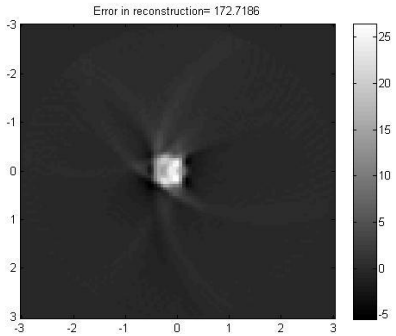

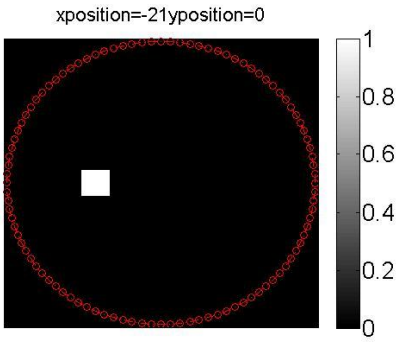

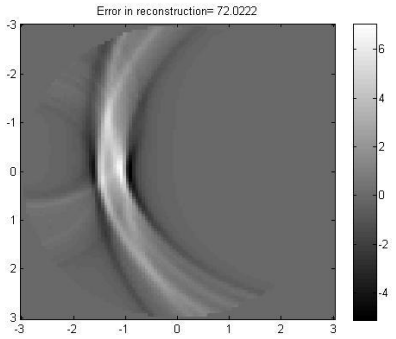

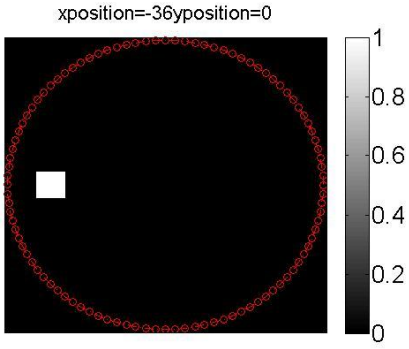

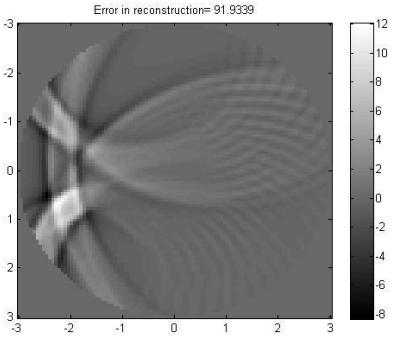

Figure 22. Phantom moved along negative x-axis while no change in y-axis

Figure 23. Phantom moved along positive x-axis while no change in y-axis

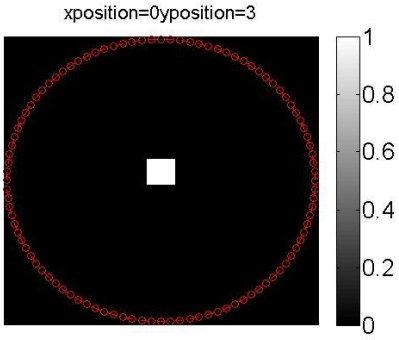

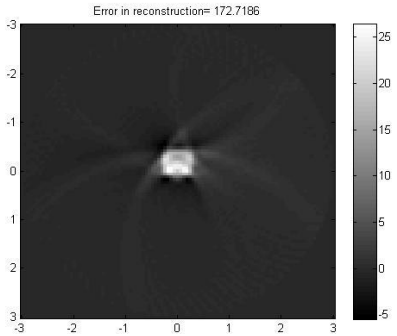

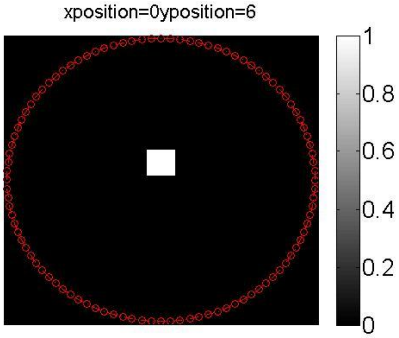

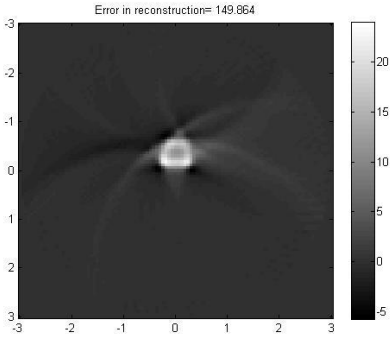

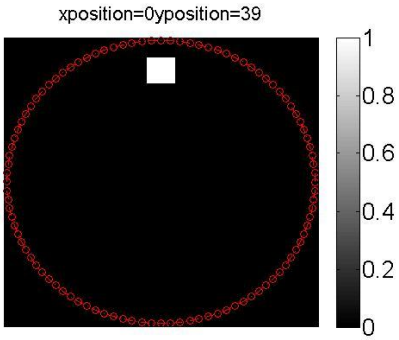

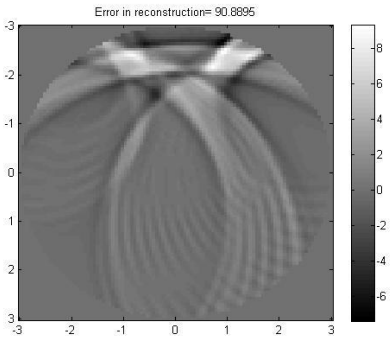

Figure 24. Phantom moved along positive y-axis while no change in x-axis

Figure 25. Corresponding reconstructions

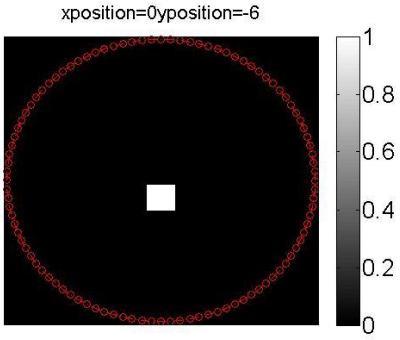

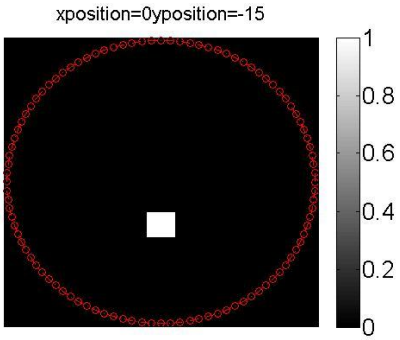

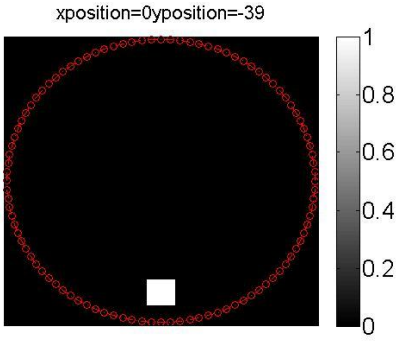

Figure 26. Phantom moved along negative y-axis while no change in x-axis

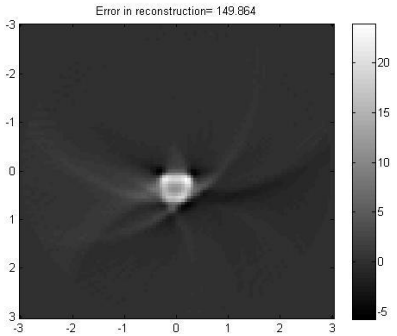

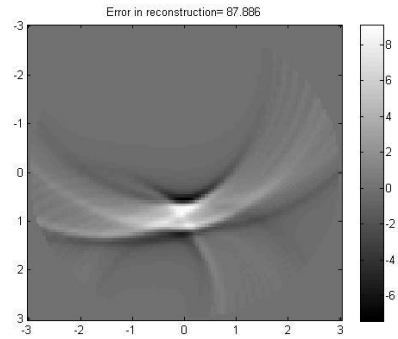

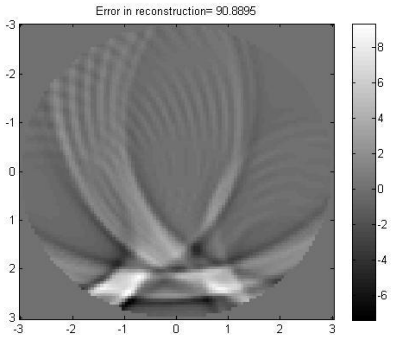

Figure 27. Corresponding reconstructions

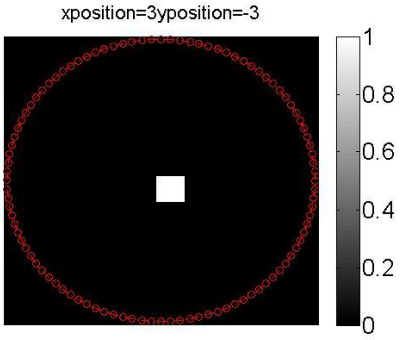

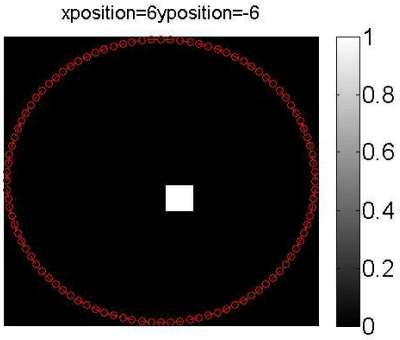

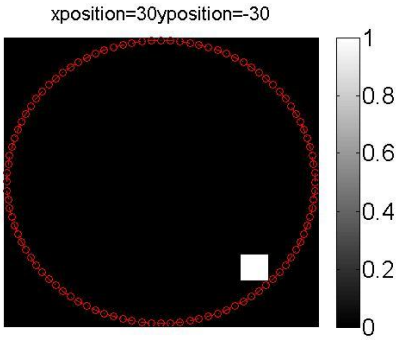

Figure 28. Phantom moved along the diagonal of the fourth quadrant of the Cartesian system

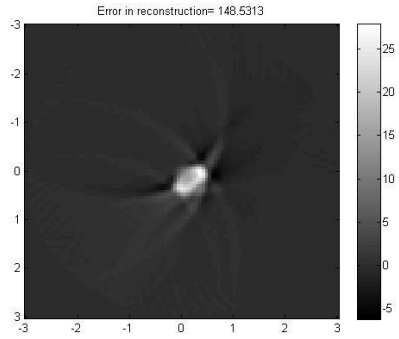

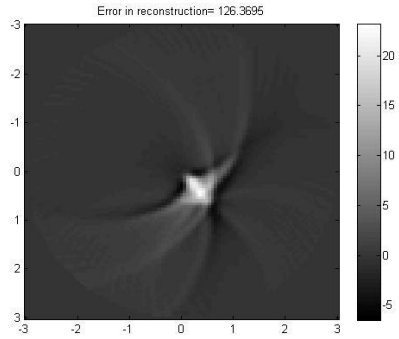

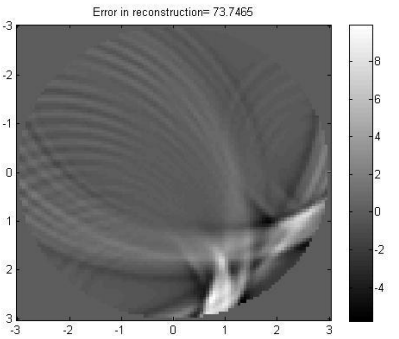

Figure 29. Corresponding reconstructions

The following phantom (figure 26) was used to find the effect of nearby objects to the original square in the binary phantom.

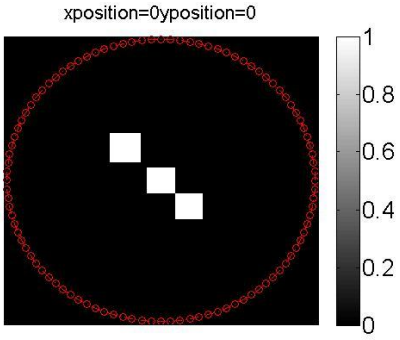

Figure 30. Objects placed next to the square in the original binary phantom

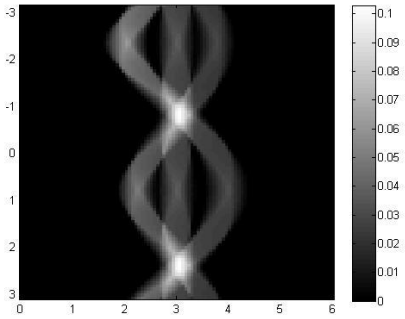

Figure 31. Corresponding sinogram

The reconstructed image is shown in Figure 32.

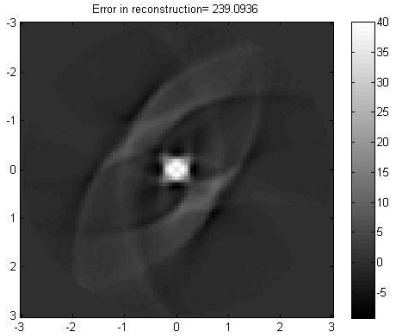

Figure 32. Reconstructed image of the phantom shown in Figure 31.

The following phantom (figure 33) was used to find the effect of the reconstruction algorithm on an asymmetrical object.

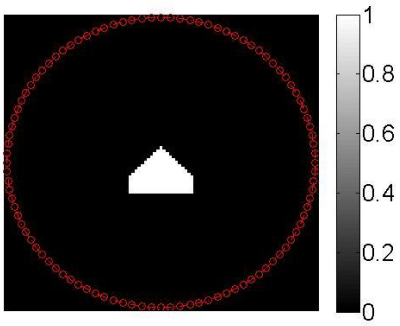

Figure 33. Objects placed next to the square in the original binary phantom

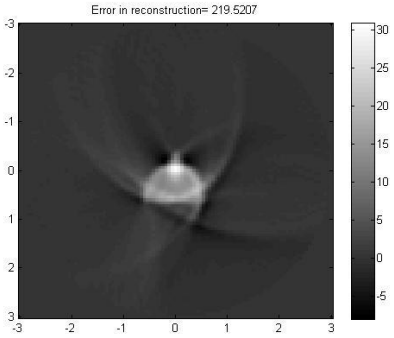

Figure 34. Reconstructed image of the phantom shown in Figure 33.

The following phantoms (figures 35 and 37) was used to find the effect of the reconstruction algorithm on the object by placing it in a random location at the top left quadrant of the Cartesian system.

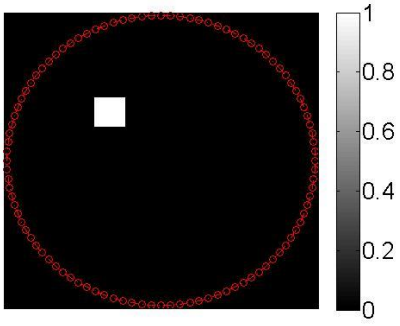

Figure 35. Objects placed in a random location on the top left quadrant

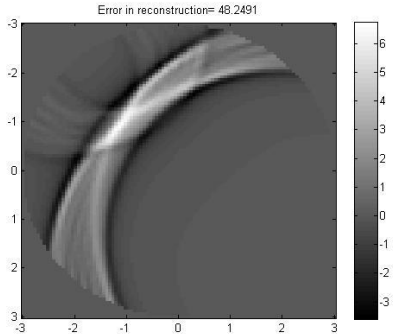

Figure 36. Reconstruction of Fig 35

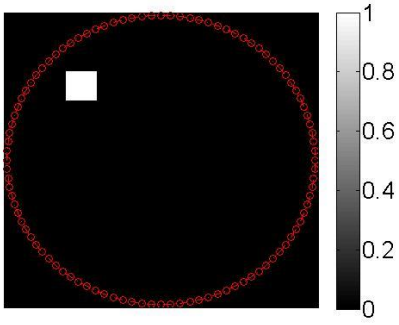

Figure 37. Objects placed in a random location on the top left quadrant

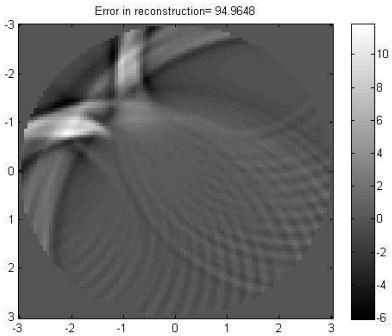

Figure 38. Reconstruction of Fig 41

The following graphs show the error in reconstruction as a function of position of the object along the x-axis, y-axis and the diagonal in the fourth quadrant of the Cartesian coordinate system.

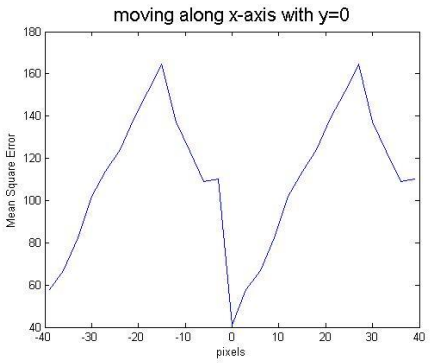

Figure 39. Error in reconstruction while phantom moved along x-axis while no change in y-axis

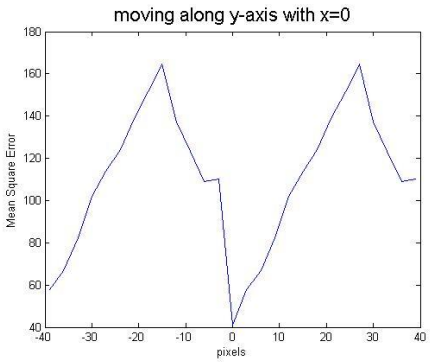

Figure 40. Error in reconstruction while phantom moved along y-axis while no change in x-axis

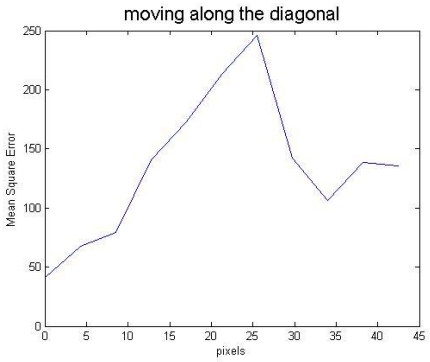

Figure 41. Error in reconstruction while phantom moved along the diagonal in the fourth quadrant of the Cartesian system

For the case of half-projections along the radial direction for all angles, the reconstruction fails to work. Figure 42, shows the sinogram for the Shepp-Logan phantom for all angles with half radial projections and Figure 40 shows the corresponding reconstruction.

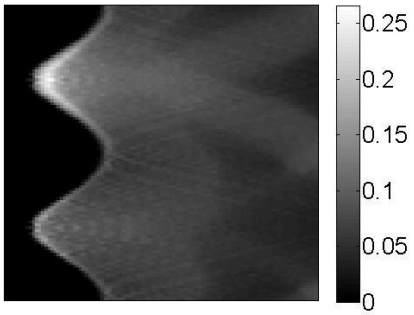

Figure 42. Sinogram for the Shepp Logan for half projections in the radial direction

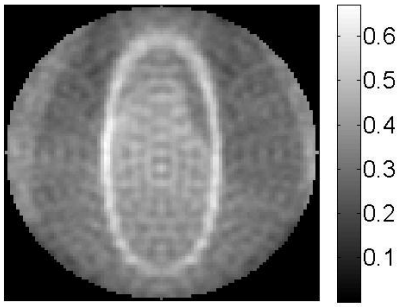

Figure 43. Recosntruction for the sinogram shown in Figure 42

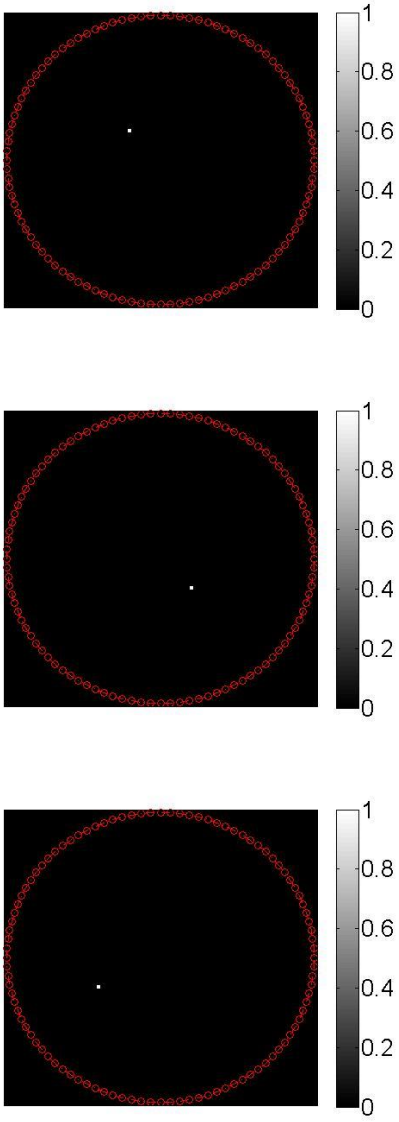

Figure 44. Moving point source around the origin

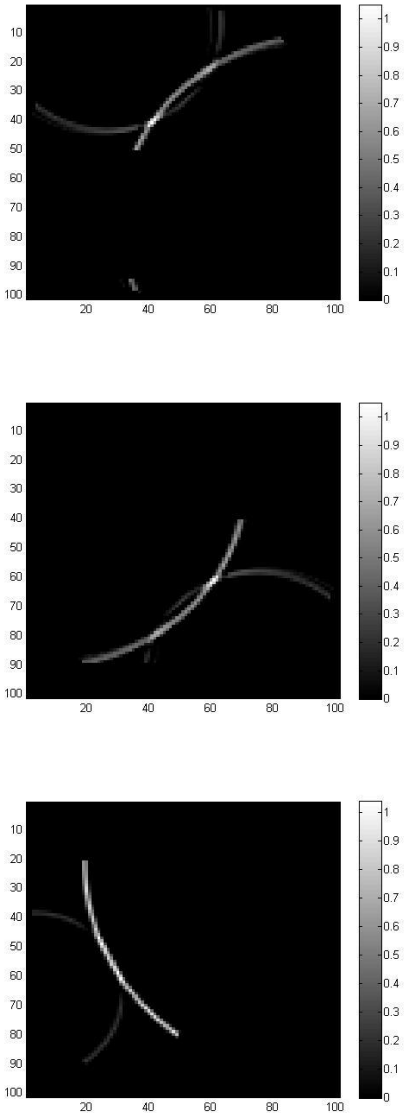

Figure 45. Corresponding reconstructions

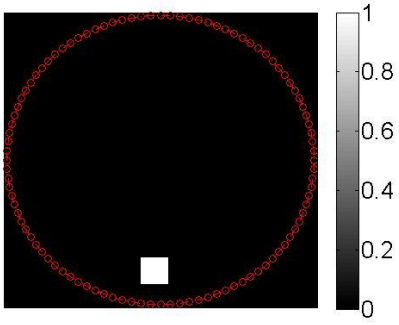
1
0.8
0.6
0.4
0.2
0

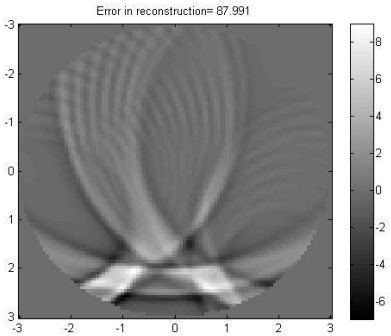
Error in reconstruction= 87.991

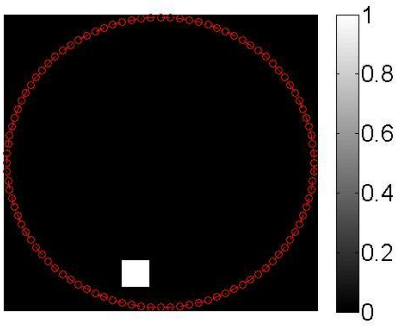
1
0.8
0.6
0.4
0.2
0

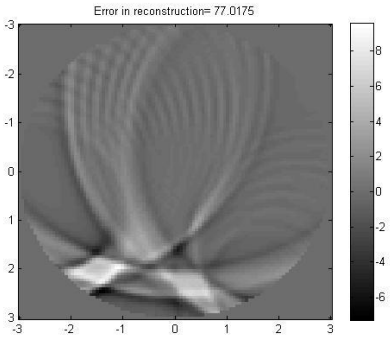
Error in reconstruction= 77.0175

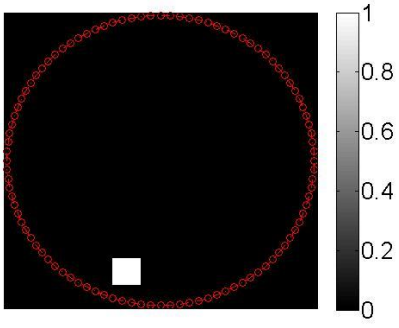
1
0.8
0.6
0.4
0.2
0

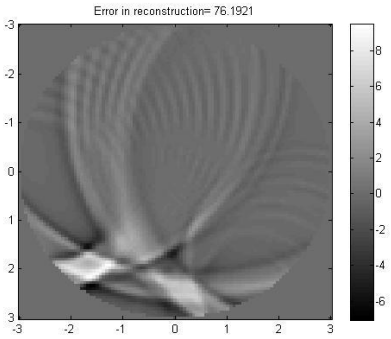
Error in reconstruction= 76.1921

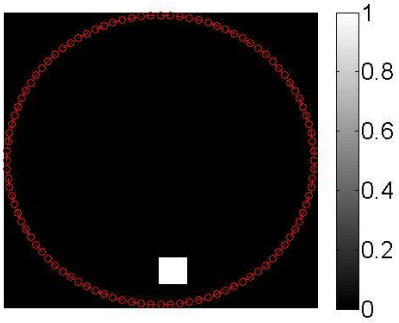

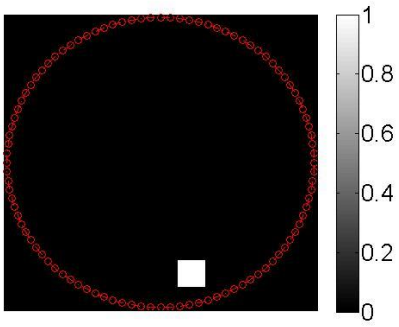

Figure 46. Moving the phantom to understand the symmetry in artifacts

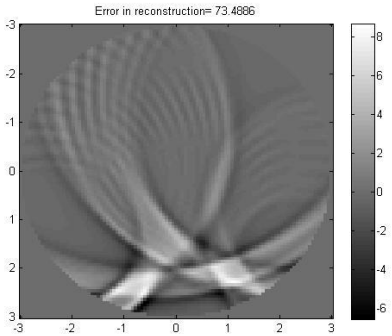

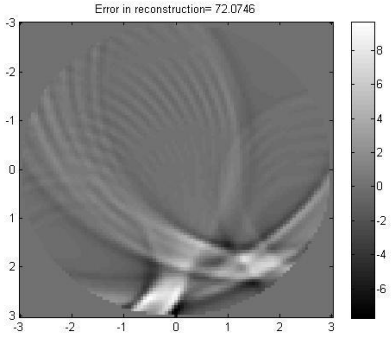

Figure 47. Corresponding reconstructions

In the case of bistatic imaging, where the radial factor in the original filter was replaced by minor axis of the ellipse over which the object is being integrated, it can be noticed that the reconstruction is favorable when the object is more towards the center of the ring of detector pairs. When the object is being displaced from the center, the reconstruction

worsens and only the artefacts are being reconstructed. This is evident from figures 26, 28 and 30.

When other squares are being added around the original object, the reconstruction still favors the square in the middle of the ring of detector pairs. The worsening of the artefacts spatially suggests that the filter (which is a log function of space) influences the reconstruction.

We can notice from figures 40 and 41 that the artefacts in the reconstruction of a point source placed at arbitrary locations around the origin splits asymmetrically which could be attributed the nonlinear nature of the filter and its effect on back smearing the obtained data.

To further understand the asymmetry, the binary square phantom was moved five pixels to left and right of the y-axis while keeping the center of the phantom around 35 pixels constantly below the x-axis. A slight flip shift in the intensities in the asymmetry could be observed between the reconstructions of the phantom on the extreme right and extreme left. A rotation of artefacts is observed while the phantom is moved from laft to right in a translational way..While the forward Radon is a linear operation, the backprojection filter does not have a linear property. And the approximation from the radial factor in the spherical Radon to the minor axis in the elliptical Radon worsens the artefacts.

Though a reconstruction technique was attempted in Mensah[48], the work fails to analytically backup the reconstruction formula. The paper mentions classical Radon backprojection which cannot be applied to elliptical Radon because a Fourier slice

theorem does not exist for elliptical Radon transformed projections. Moreover, the reconstruction techniques mentioned in the paper fails to satisfy the special cases of ellipse namely, the line and the circle. When the two foci move away to infinity an ellipse become a line and the corresponding Radon becomes the classical Radon. But the parameterization of the lines in the classical Radon are in a different direction as compared to this special case of ellipse. A classical reconstruction would not work in this scenario. In the case when the two foci come together, the ellipse becomes a circle and the filter used in this paper does not match the analytically derived filter in Finch[47].

CHAPTER V

CONCLUSION AND FUTURE WORK

In the most common scenario Transrectal Ultrasound is performed using an endorectal probe containing linear arrays[50]. The primary contrast agent in the conventional imaging is the acoustic impedance mismatch. Acoustic impedance depends on the velocity and density and hence the tissue boundaries where these properties change will produce image contrast. Scatterers smaller than the wavelength can produce speckles in the ultrasound image.

Unfortunately, intracapsular prostate cancer is difficult to detect with standard 2D ultrasound. First, the prostate is a much more homogeneous tissue than the breast, and hence the contrast is limited. Furthermore, prostate cancer has a wide variation in appearance that overlaps with the appearance of other benign pathologies and hence conventional 2D ultrasound has not been shown to provide any additional sensitivity compared to digital rectal exam (DRE).

Since the progression of prostate cancer is an inherently 3D process, imaging the prostate in 3D may be useful for a radiologist. 3D TRUS is one way of imaging 3D prostate but still will suffer from contrast issues. Contrast-enhanced prostate Sonography using microbubbles has shown potential for prostate cancer detection and diagnosis[51].Although

the prostate is not as well-vascularized as the breast, there is sufficient capacity to even perform dynamic wash in/out studies using commercial microbubbles.

There also been some research work on translating transurethral ultrasound (TUUS) from therapeutic modality[52] to an imaging modality[53]. The image formation methods are different between TUUS and TRUS, novel methods can be invented combining these two.

In applications of breast imaging, photoacoustic and thermoacoustic tomography have been successful and powerful. Both these modalities merge a non-ionizing, high contrast/poor-resolution with low contrast/high resolution ultrasound to produce high quality images. However, there are technical obstacles in implementing these techniques in 3-D

In the pulse-echo method the axial resolution is inversely related to the ultrasound frequency For example to detect a 150μm sized breast microcalcification, frequencies greater than 10 MHz must be used. Higher the frequency, more they are attenuated in the body by tissues. In applications like breast imaging, reflection and transmission tomographic techniques are geometrically well-suited. Reflection tomography could be corrected for diffraction though it suffers the resolution limits like the pulse-echo methods. In transmission tomography, the Fourier diffraction tomography principle and related filtered backprojection image reconstruction algorithm can be used to produce good quantitative images of tissue attenuation and velocity[8].But they are not sensitive to hard scattering by some microcalifications Recent advances in inverse scattering

techniques are applied for breast imaging. Since the breast cannot be surrounded by detectors, as used in photoacoustic tomography, an additional angular coverage may be inherent to the collected acoustic data.

In time-domain ultrasound tomographic imaging, there exist several quantitative image reconstruction techniques. But there are limitations with FBP based techniques that reconstruct the object from integral transformed projections. One of the limitations is that all of the filtered back projection algorithms that currently exist work only if the compact of the image space is well-defined. This means that the image space is zero outside a fixed domain. This results in severe artefacts when we try and reconstruct objects that are placed exterior to the ring of detectors as shown in Figure 14. Even the reconstruction techniques suggested in[47] result in high smoothing of the object as is apparent from Figure 9 due to the log based radial filter. An additional limitation with the Radon transformed image reconstruction is that it works only when the medium is insonified by an impulse (which means infinite bandwidth). This might result in additional artefacts while reconstructing real data.

For the case of half-view data acquisition, that is, data obtained by detectors placed on a semi-circular arc around the object, the algorithm reconstructs surfaces that are touched tangentially by the circles over which they are integrated. This is evident from figure 15. It can be noticed that the sides of the squares disappear in the reconstruction. A mathematical discussion for this case can be found in[49].

As part of the future work, as a mathematical pursuit, an analytical formula to reconstruct elliptical Radon transformed data can be approached. In a special case of the elliptical Radon, a parabolic Radon can be obtained by moving one of the detectors to infinity, that is to say, keeping one of the foci of the ellipse constant and moving the other to infinity. An analytical formula for reconstruction for this case is currently not available in literature.

From an engineering perspective, reconstruction from limited number of angular projections can be approached. This will translate to lesser number of detectors in practice. Moreover, all the reconstruction algorithms assume that the speed of sound is constant. A more realistic model can be approached with varying speed of sound in an heterogeneous medium. With an integral type modeling, this will lead to a Radon transform in a different surface. It may be called the ‘noisy’ Radon. An adaptive filter to backproject this kind of data can also be approached.

APPENDIX A

Matlab Code for forward and backprojection of Spherical Radon

```
%Sradon.m need to be run with integrate1.m
%I would like to thank Marcus Haltmeier (email:
markus.haltmeier@uibk.ac.at) for sharing a partial pseudo-code and
%helping me understand the paper better

fun=phantom(101); %Insert your phantom here
radius=3;
diameter=2*radius;
angles=100;
radial=100;
sinogram=zeros(angles,radial+1);
angle_inc= 2*pi / angles;
radial_inc  = diameter/ radial;
object=linspace(-3,3,101);
object1 = linspace(-3,3,angles);
fil =linspace( 0,12,201);
fil=fil(:);
lfil=length(fil)-1;
dfil=fil(2)-fil(1);
pixel=object1(2)-object1(1)  ;
[X,Y]=meshgrid(object,object);
FINAL = zeros(101);
nfil=linspace(0,lfil-1,lfil)';
a=zeros(lfil+1,lfil);
b=zeros(lfil+1,lfil);


for i=1:lfil+1
    filtemp=fil(i) ;
    k =i-1;
    g1=-log(abs((nfil+1-k)./(nfil-k)));
    g1(i)=0;
    g2 =-filtemp*log(abs((nfil+1-k)./(nfil-k) ) );
    g2(i) = 0;
    if k>0
        g1(i-1) = 0;
        g2(i-1) = 0;
    end
    a(i,:)=g1(1:lfil);
    b(i,:)=g2(1:lfil)-fil(1:lfil).*g1(1:lfil);
end
```

```
object  = linspace( -3, 3, 101 );
ang = linspace( -pi, pi - 0.001, angles );
rad  = linspace( 0,diameter, radial+1);
xcirc = diameter/2 * cos(ang);
ycirc = diameter/2 * sin(ang);


for i=1:angles
center=[xcirc(i) ycirc(i)];
gram1 = integrate1( center,radius,fun,rad );
sinogram( i,: ) = gram1(1,:);
end

imagesc(sinogram);
radial1=radial-1;

for backp =1:angles
    cent   = [xcirc(backp); ycirc(backp)  ];
    mf(1,1:101 ) = sinogram(backp,1:101 )  ;

  mf(2:end-1)  = (mf(3:end) - mf(1:end-2))/(2*(radial_inc));
  mf = rad.*mf;
   if(backp==10)
        kk=mf;
    end
   m = [  -mf(end:-1:1) , mf(2:1:end) ];
   m = m(1:200)*a' +((m(2:201)-m(1:200) )/radial_inc)*b';
    mf(1,1:1:101) = m(1,101:1:201);
    dist=sqrt((X-cent(1)).^2+(Y-cent(2)).^2);

    fun1=interp1(rad,mf,dist) ;
   %
    FINAL=FINAL+fun1;
end
FINAL = (3*2*pi/100)*FINAL/(2*pi*3);
FINAL(not(FINAL<Inf))=0;
figure(2);
imagesc(FINAL);


%integrate1.m

function gram1 = integrate1(center,radius, fun,rad );

object = size(fun, 1 ) - 1;
xV = linspace(-radius,radius, object+1 );
```

```
mf = zeros( size(rad) );

hh = floor( 2 * object *  pi );

summe = 0;
for ir = 1:length(rad)
    r0 = rad( ir );

   beta= real( acos( r0 / (2*radius) ) ) ;
    calc  = atan2( center(2) , center(1) );
    hh2 = floor( hh * (beta/pi) * r0/(2*radius) ) + 1;
     angleV = linspace(calc+pi - beta, calc+pi + beta, hh2);
    s1 = center(1) + r0*cos( angleV );
    s2 = center(2) + r0*sin( angleV );

    fw  = interp2( xV, xV', fun, s1, s2 );
    fw( not(fw < Inf) ) = 0;
    summe = sum(fw(:));

    gram1(ir) = summe;
end
```

REFERENCES

1. Bjorn A.J. Angelsen, Ultrasound Imaging – waves, signals and signal processing, J. Acoust. Soc. Am, 121 (4), pp.1820-1820, 2007.
2. Frank Natterer, “An algorithm for 3D ultrasound tomography”, Inverse problems of wave propagation and diffraction, pp.216-225, Springerlink, 2007.
3. S. J. Norton and M. Linzer, Ultrasonic reflectivity tomography: Reconstruction with circular transducer arrays, Ultrason. Imaging, 1, pp.154-184, 1979.
4. S.J.Norton and M.Linzer, Ultrasonic reflectivity imaging in three dimensions: Reconstruction with spherical transducer arrays, Ultrason. Imaging, 1, pp.210-231, 1979.
5. M.Kaveh, R.K.Mueller, and R.D.Iverson, Ultrasonic tomography based on perturbation solutions of the wave equation, Comput. Graphics and Image Processing,9,pp.105-116,1979
6. R.K. Mueller, M.Kaveh, and G.Wade, Reconstruction tomography and applications to ultrasonics, Proc. IEEE, 67, pp.567-587, 1979.
7. R.K.Mueller, M.Kaveh, and R.D.Iverson, A new approach to acoustic tomography using diffraction techniques, Acoustical holography, 8, A.Metherell, Ed. New York: Plenum, pp.615-628, 1980.
8. S.K.Lehman and S.J.Norton, Radial reflection diffraction tomography, J. Acoust. Soc. Am, 116(4), pp.2158-2172, 2004.
9. P.N.T.Wells, Biomedical Ultrasonics, Academic Press, 1977.
10. R.K.Mueller, M.Kaveh, and R.D.Iverson, A new approach to acoustic tomography using diffraction techniques, In: A. Metherall, Editor, Acoustical Imaging, Plenum Presspp.615-628, 1980.
11. E.Wolf, Three-dimensional structure determination of semitransparent objects from Holographic data, Optics Commun., pp.153-156, 1969.
12. J.F.Greenleaf *et al.,* Algebraic reconstruction of spatial distributions of acoustic velocities in tissue from their time-of-flight profiles, Acoustic Holography, 6, pp.71-90, 1975.
13. J.F.Greenleaf, S.A.Johnson,S.L.Lee,G.T.Herman, and E.H.Wood, Algebraic reconstruction of spatial distributions of acoustic absorption with tissues from their two-dimensional projections, Acoustical Holography, edited by P.S.Green(Plenum, New York),5,pp.591-603,1974.
14. R.K.Mueller, Diffraction Tomography I: The wave equation, Ultrason. Imag. , 2, pp.213-222, 1980.
15. E.Wolf, Three dimensional structure determination of semitransparent objects from holographic data, Opt. Commun.,1(4),pp.153-156,1969.

16. K.Iwata and R.Nagata, Calculation of refractive index distributions from interferograms using Born and Rytov's approximation, Jap. J. Appl. Phys, 14, pp.379-383, 1975.
17. J.M.Tribolet, A new phase unwrapping algorithm, IEEE Trans. Acoustics. Speech. Signal Proces. ASSP-25(2), pp.170-197, 1977.
18. S.A.Goss, R.L.Johnston, and F.Dunn, Comprehensive compilation of empirical ultrasonic properties of mammalian tissues, J. Acoust. Soc. Am., 64(2), pp.423-457, 1978.
19. S.A.Goss, R.L.Johnston and F.Dunn, Compilation of empirical ultrasonic properties of mammalian tissues. II, J. Acoust. Soc. Am., 68(1), pp.93-108, 1980.
20. S.J. Norton, Reconstruction of a reflectivity field from line over circular paths, J. Acoust. Soc. Am., 67(3), pp, 853-863, 1980.
21. S.J. Norton, Theory of acoustic imaging, Ph.D. thesis, Stanford University, Stanford Elect. Lab. Tech. Rept. No.4956-2, Chap. 5, 1976.
22. A. G. Bell, On the production and reproduction of sound by light, Am. J. Sci., 20, pp.305-324, 1880.
23. C. K. N. Patel and A. C. Tam, Pulsed optoacoustic spectroscopy of condensed matter, 53, pp.517-550, 1981.
24. M.Xu and L.V. Wang, Photoacoustic imaging in biomedicine, Rev. Sci. Inst.,77,pp.041101(1-22),2006.
25. G.Ku, X.wang, G.Stoica and L.-H.Wang, Multiple bandwidth photoacoustic tomography, Phys. Med. Biol., 49(7), pp.1329-1338, 2004.
26. F. A. Duck, Physical properties of tissue, Academic, London, 1990.
27. J.C. Lin, On microwave-induced hearing sensation, IRE. Trans. Microwave. Theory Tech., MTT-25, pp.605-613, 1977.
28. V.E. Gusev and A.A. Karabutov, Laser optoacoustics, American Institute of Physics, New York, 1993.
29. Photons plus ultrasound: Imaging and sensing 2005, edited by A.A Oraevsky and L.V.Wang (SPIE, Bellingham, WA, 2005), vol.5697.
30. Photons plus ultrasound: Imaging and sensing 2006, edited by A.A Oraevsky and L.V.Wang (SPIE, Bellingham, WA, 2006), vol.6086.
31. M. Haltmier, O. Scherzer, P. Burgholzer, and G. Paltauf, Thermoacoustic computed tomography using large planar receivers, 20(5), pp.1663-1674, 2004.
32. A. C. Tam, Applications of photoacoustic sensing techniques, 58(2), pp.381-431, 1986.
33. A.A. Oraevsky and A.A. Karabutov, in Biomedical Photonics Handbook, edited by T.Vo-Dinh (CRC, Boca Raton, FL), Chap. 34, 2003.
34. A. Macovski, Ultrasound imaging using arrays, Proc. IEEE, 67, pp.484-495, 1979.
35. F.Duck, S.Johnson, J.Greenleaf and W.Samayoa, Digital image focusing in the near field of a sampled acoustic aperture, Ultrasonics, 15, pp.83-88, 1977.

36. J.D.Coker and A.H. Tewfik, Multistatic SAR image reconstruction based on an elliptical geometry Radon transform, IEEE International conference on waveform diversity and design, pp.204-208, 2007.
37. Y. Xu, L.-H.Wang, G.Ambartsoumian and P.Kuchment, Reconstructions in limited-view thermoacoustic tomography, Med. Phys, 31, pp.724, 2004.
38. R. M. Arthur and S. R. Broadstone, Imaging via inversion of ellipsoidal projections of solutions to the linear acoustic wave equation, IEEE Trans. Med. Imag, 8(1), pp.89-95, 1989.
39. S. J. Norton, Reconstruction of a two-dimensional reflecting medium over a circular domain: Exact solution, J. Acoust. Soc. Am., 67(4), pp.1266-1273, 1980.
40. S.J.Norton and M.Linzer, Ultrasonic reflectivity imaging in three dimensions: Exact inverse scattering solutions for plane, cylindrical, and spherical apertures, IEEE Trans. Biomed. Engg., 28(2), pp.202-220,1981.
41. S.Aks and D.J.Vezzetti, Ultrasonic scattering theory I: Scattering by single objects, Ultrason. Imaging, 2, pp.85-101, 1980.
42. J.Ball, S.A.Johnson, and F.Stenger, Explicit inversion of the Helmholtz equation for ultrasound insonification and spherical detection, Acoustical Holography,8,A.Metherell, Ed. New York: Plenum, 1980.
43. G. Barton, Elements of Green's functions and propagation – Potentials, diffusion and waves, Oxford University Press, 1991.
44. S.Pourjavid and O. Tretiak, Ultrasound imaging through time-domain diffraction tomography, IEEE Trans. Ultrason. Ferroelectr. Freq. Control, 38, 74-85, 1991.
45. T. D. Mast, Wideband quantitative ultrasonic imaging by time-domain diffraction tomography, J. Acoust. Soc. Am., 106(6), pp.3061-3071, 1999.
46. J.M. Blackledge, R.E.Burge, K.I.Hopcraft and R.J.Wombell, Quantitative diffraction tomography: I. Pulsed acoustic fields, J. Phys. D., 20, pp.1-10, 1987.
47. D.Finch, M.Haltmeier and Rakesh, Inversion of spherical means and the wave equation in even dimensions, SIAM J. Appl. Math., 68(2), pp.392-412, 2007.
48. S.Mensah and E.Franceshini, Near-field ultrasound tomography, J. Acoust. Soc. Am., 121(3), pp.1423-1433, 2007.
49. P.Kutchment and L.Kunyansky, A survey in mathematics for industry: Mathematics of thermoacoustic tomography,Euro. Jnl. Of Appl. Mathematics,19, pp.191-224,2008.
50. ACR, ACR Practice guideline for the performance of ultrasound evaluation of the prostate (and surrounding structures), pp.1035-1038. ACR, 35 edition, 2006.
51. Ethan J Halpern, Contrast-enhanced ultrasound imaging of prostate cancer, Rev. Urol., 8(suppl 1): S29-S37, 2006.

52. C. Diedrich and E. C. Burdette, Transurethral ultrasound array for prostate thermal therapy: Initial studides. IEEE trans. On Ultrasonics, Ferroelectrics and frequency control, 43(6), pp.1011-1022, 1996.
53. J.O.Salo, T.Lehtonen and S.Rannikko, Prostate cancer protruding into the bladder imaged by transurethral and transrectal ultrasound, International journal on Nephrology, 19(2), pp.171-174, 1987.